

Low radio frequency observations of seven nearby galaxies with GMRT

Subhashis Roy¹  Souvik Manna¹

¹*National Center for Radio Astrophysics, TIFR, Pune University Campus, Ganeshkhind, Pune 411007, India*

26th August 2021

ABSTRACT

We have observed seven nearby large angular sized galaxies at 0.33 GHz using GMRT with angular resolution of $\sim 10''$ and sub-mJy sensitivity. Using archival higher frequency data at 1.4 or ~ 6 GHz, we have then determined their spatially resolved non-thermal spectrum. As a general trend, we find that the spectral indices are comparatively flat at the galaxy centres and gradually steepen with increasing galactocentric distances. Using archival far infrared (FIR) MIPS $70 \mu m$ data, we estimate the exponent of radio-FIR correlation. One of the galaxy (NGC 4826) was found to have an exponent of the correlation of ~ 1.4 . Average exponent from 0.33 GHz data for the rest of the galaxies was 0.63 ± 0.06 and is significantly flatter than the exponent 0.78 ± 0.04 obtained using 1.4 GHz data. This indicates cosmic ray electron (CRE) propagation to have reduced the correlation between FIR and 0.33 GHz radio. Assuming a model of simple isotropic diffusion of CRE, we find that the scenario can explain the frequency dependent cosmic ray electron propagation length scales for only two galaxies. Invoking streaming instability could, however, explain the results for the majority of the remaining ones.

Key words: galaxies: ISM, galaxies: individual, radio continuum: galaxies, cosmic ray electrons.

1 INTRODUCTION:

Emission from galaxies acts as a tracer of energetic processes. Different physical processes cause emission to peak in different wavebands. Low radio frequency emission mostly originates from non-thermal emission due to acceleration of high energy cosmic-ray electrons (CREs) in the ambient galactic magnetic fields. Thus the diffuse radio non-thermal emission traces the journey of the CRE from the production site to different parts of the galaxy. Cosmic ray production is linked to star formation rates (SFRs) through supernovae, and stars act as the main source of energy in galaxies. Therefore, studying low radio frequency emission at high angular resolution from different parts of a galaxy could provide important information not only of SFRs, but also on how the CREs diffuse from their place of origin and their interaction with other components of the interstellar medium (ISM) and the strength of magnetic fields.

There have been significant number of observational studies of radio emission from nearby large galaxies and to characterise the propagation of CREs in them. Generally the

observed radio emission is a mixture of thermal and non-thermal emission. Thermal emission in galaxies is mostly seen to originate from dense ionised gas in star forming regions (typically in galactic arms), and the nonthermal emission arises from acceleration of CREs originating in supernova shocks (e.g., van der Kruit 1971; van der Kruit et al. 1977; Hummel 1981; Beck & Graeve 1982; Condon 1992; Berkhuijsen et al. 2003; Paladino et al. 2009; Beck et al. 2020). These observations also established that the non-thermal spectral index is of about -0.5 close to star forming regions, which is flatter than the spectral index of ~ -0.75 in non star-forming regions which is expected from the model of CRE acceleration (e.g., Bell 1978; Biermann & Strom 1993). As the CREs propagate away from their origin, they lose energy by several processes including synchrotron, inverse Compton and ionisation. Among these, at low radio frequencies as presented here, energy loss by synchrotron process dominates from most parts of typical nearby star forming galaxies (Basu et al. 2015). CREs can propagate away through physical processes like diffusion, streaming instability and outflow (advection). Radio spectra becomes steeper for regions away from the major star forming regions (e.g., interarm) due to higher relative loss of

* email: roy@ncra.tifr.res.in

energy from high energy CRes, whose energy goes down faster with time (Basu et al. 2012a). The radio emission is not only confined to the galactic disk, but several sensitive studies have shown many spirals to have significant halo emission reaching kpc distances above the disk (e.g., Hummel & van der Hulst 1989; Hummel & Dettmar 1990; Hummel 1991; Rossa & Dettmar 2003; Irwin et al. 2012; Krause et al. 2018).

In star forming regions, both UV photons and CRes are generated. The UV photons in turn can heat up dust which then re-radiates in the far infra-red (FIR) band (e.g., Helou et al. 1985; Condon 1992). Radio emission originates from CRes in presence of magnetic fields which increases in dense star forming regions. The above physical parameters are believed to give rise to the radio-FIR correlation, which is one of the tightest correlation in astrophysics that holds over five orders of magnitude in both radio and FIR luminosities (e.g., Condon 1992; Yun et al. 2001). This correlation holds for wide morphological class of galaxies (Wunderlich et al. 1987; Dressel 1988; Price & Duric 1992) including normal galaxies. Condon (1992) have studied this correlation in normal galaxies in global scale using FIR band IRAS 60 μm and 100 μm FIR flux densities (Helou et al. 1988) and 1.4 GHz radio flux densities and found excellent correlation and a dispersion of less than 0.2 dex. Yun et al. (2001) have found this correlation between monochromatic far-infrared luminosity (60 μm) and 1.4 GHz radio luminosity. Radio-FIR correlation also holds good at kpc scales (e.g., Murgia et al. 2005; Tabatabaei et al. 2007a; Xu et al. 1992). Linear correlation was found between thermal radio emission and warm dust emission for LMC (Hughes et al. 2006). Non-thermal radio emission and cool dust emission were found to be correlated in non-linear fashion for M31 (Hoernes et al. 1998). Dumas et al. (2011) found the exponent of the radio-FIR correlation to vary among centre, arm, interarm and outer regions for the galaxy. Several models exist to explain the correlation starting from global to parsec scales. Assuming galaxies to be optically thick, calorimeter model (Voelk 1989; Lisenfeld et al. 1996) can explain global correlation for many galaxies but fails to explain the local scale correlation. Non-calorimeter model by Niklas & Beck (1997) considered diffusion, radiative decay and finite escape probability of cosmic rays and it can explain local scale correlation for optically thick and thin regime of dust heated by UV photons. Radio-FIR correlation in smaller scales in galaxies are governed by CRe propagation scale (Tabatabaei et al. 2013). More recently, Heesen et al. (2019) found different exponent in radio-FIR correlation for steep and flat spectrum regions in four nearby spirals. They also studied the CRe propagation lengths at 0.14 and 1.4 GHz in these galaxies.

Though a large number of studies on nearby spirals have been made, most of these studies were performed at frequencies of 1.4 GHz and above, or had low resolution at lower frequencies (e.g., $\sim 1'$ with WSRT at 0.33 GHz). To find the common properties of these galaxies and to compare them with different galaxy types, observing a complete set of galaxies is needed with high resolution at lower frequencies. For example at metre wavelengths, due to longer lifetime, CRes can propagate to a few kpcs from their origin. As a result the spatially resolved radio-FIR correlation at resolution below 1 kpc could be destroyed. This effect can be tested via spatially resolved radio-FIR correlation at

each radio frequency. For galaxies within ~ 10 Mpc, 1 kpc corresponds to an angular scale of $\gtrsim 30''$, which can be measured with an interferometer with a resolution of $\sim 10''$. As CRes can propagate through diffusion, streaming instability and through advection, the above in conjunction with higher frequency observations could provide important clues for propagation of CRes in nearby galaxies (Heesen et al. 2018; Vollmer et al. 2020). There have been only a few studies of spatially resolved radio-FIR correlation in nearby large galaxies utilising radio data below 1 GHz. The study by Basu et al. (2012b) found the radio-FIR exponent between 0.33 GHz and 70 μm of four large nearby spirals to be flatter as compared to using 1.4 GHz data. However, their study included only four large spirals, and to generalise the above trends, enlarging the sample size is required. To facilitate such a study, we have made a sample of 46 galaxies within 11 Mpc. Seven of these galaxies have been observed with the Giant Metrewave Radio Telescope (GMRT) at 0.33 GHz as a pilot project, the results of which are presented in this paper. Sample selection is presented in Sect. 2, observational details and data reduction are described Sect. 3. In Sect. 4, we present the results of our observations including radio maps at 0.33 and 1.4 GHz, their spatially resolved spectrum, properties of the individual galaxies, radio-FIR correlation and a simple model of cosmic ray propagation. Discussions are presented in Sect. 5, and conclusions are drawn in Sect. 6.

2 SAMPLE SELECTION

Spitzer Local Volume Legacy (LVL) is a complete volume limited sample of 258 galaxies within 11 Mpc (Dale et al. 2009). For most of these galaxies, UV, H α , optical and multi-frequency IR observations have been made. To carry out Giant Metrewave Radio Telescope (GMRT) observation we selected 46 out of 258 galaxies of LVL sample based on the following criteria:

(i) To have large number of resolution elements across the galaxies, we selected galaxies with angular size larger than $6'$. (ii) To minimise the zero spacing missing flux problem of an interferometer like GMRT with shortest spacing of $\sim 50 - 100\text{m}$, we used an upper cut-off of $17'$ ($\leq 20\%$ missing flux at the shortest spacing for Gaussian intensity distribution). (iii) Declination greater than -45° , so that they are visible from the telescope site for > 5 hours a day, which allows for better uv-coverage through Earth rotation synthesis.

3 OBSERVATIONS AND DATA ANALYSIS:

3.1 GMRT observation

We observed 7 out of 46 selected galaxies with GMRT as pilot observations at 0.33 GHz with a bandwidth of 32 MHz. A total of 512 frequency channels were used across the observing band and typical on source observing time was $\sim 3 - 5$ hours. Details of observations are given in Table-1. For making final images the data was analysed in various methods as mentioned below. For the galaxy NGC 2683, data editing, calibration, self-calibration and imaging was performed by using the pipeline SPAM (Source Peeling and Atmospheric Modelling by Intema (2014)). In this

case, 3C286 was used as the primary calibrator. For all other sources, initial data editing and calibration were performed by following the standard approach in Astronomical Image Processing System (Aips), where 3C286 was used as the primary calibrator. Phase calibration was performed using observation of a P-band calibrator chosen from VLA calibrator manual such that its angular distance is within 15 degrees from the target source. It was observed periodically every ~ 30 minutes. The calibrated data for NGC 3627, 4096, 4449 and 4490 were self calibrated and imaged using SPAM. Imaging of NGC 4826 and 5194 were done manually in Aips. The initial images of these two sources were improved by phase only self-calibration. Finally, while doing A&P self calibration, overall gains were normalised to unity with solution interval of 10 minutes. To make the final images of the extended images along with the compact sources with better fidelity than the standard Clean algorithm, we employed a variant of multi-resolution Clean (Wakker & Schwarz 1988) using the task IMAGR in Aips. From the self-calibrated UV data, we made (i) multi-facet images of compact sources with high resolution using a short UV cutoff such that the Central Square baselines ($\lesssim 1$ km) of GMRT (Swarup et al. 1991) are not used during imaging. Then the significant Clean components are removed from the UV data used in stage (ii). A low resolution image of the field is made in stage (iii) from the data produced in (ii) with UV range corresponding to Central Square baselines. During Clean in step (iii), extended Gaussian components of FWHM about 0.5 times of resolution of the image are used. Since the resolution of the image produced in (iii) is pretty low, a single facet for the whole field could be used. In stage (iv), the Clean components produced in stage (iii) are subtracted from the original self-calibrated UV data. Using the low resolution Clean component subtracted UV data, another set of multi-facet images are made in stage (v) without any short UV cutoff. Since most of the extended sources are removed through low resolution imaging in stage (iii), these images do not show the typical instability exhibited by the Clean algorithm for extended sources. To produce the final image, the Gaussian Clean components subtracted in stage (iv) are added back to the image produced in stage (v). The technique described above uses a single facet for low resolution Clean with cell-size of ~ 4 smaller than the low resolution beam (stage iii). However, IMAGR in Aips uses the same cell size in low resolution Clean as is done in high resolution. Use of a much larger cell-size in low resolution Clean significantly speeds up the deconvolution process as compared to the one in IMAGR. To measure rms noise in the images made, we used the Aips task IMEAN, which fits a Gaussian noise profile to histogram made using the pixel value distribution. When the image concerned is small and was from public archive, we estimated rms noise in a couple of boxes (using TVSTAT) with sizes similar to the source and made on opposite sides of the same. The quoted value is the average of the two.

3.2 Higher frequency archival data

To study propagation of CRes at higher frequencies (Sect. 4.3), to compare radio-FIR correlation with 0.33 and 1.4 GHz radio data (Sect. 4.4) and to get spectral indices for some of these galaxies we analysed VLA archival data

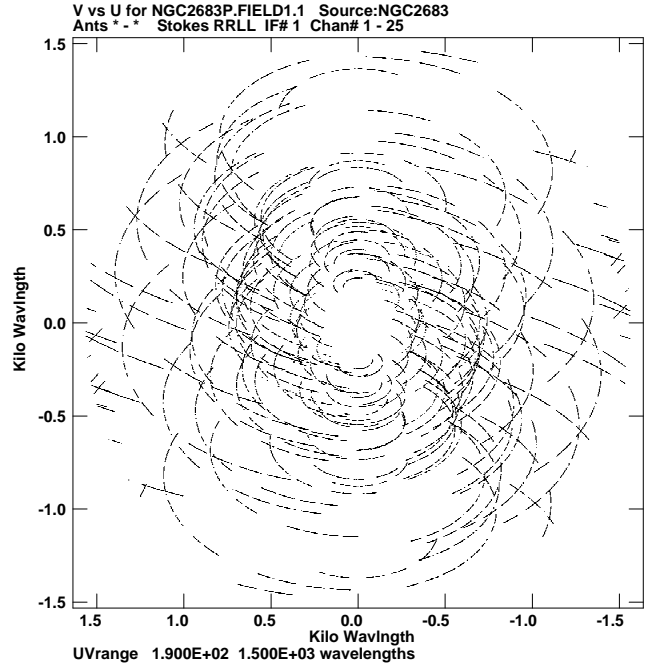


Figure 1. UV-coverage at 0.33 GHz within an uv -distance of 1.5 $k\lambda$ for the source NGC 2683.

for all the seven galaxies at L-band (~ 1.4 GHz). These data were chosen such that the minimum bandwidth was of 50 MHz and observing time was more than 20 minutes. Though the resolution of the GMRT images from UV data without any cutoffs are high ($\sim 10''$, Table-1), to get reasonably good ($\gtrsim 5$) signal to ratio for extended emission of the galaxies (e.g., for making spectral index images of extended emission), somewhat lower resolution was needed. Also, the propagation of CRes are studied through radio-FIR correlation (Sect. 4.3), where $70 \mu\text{m}$ Spitzer FIR data has a resolution of $18''$. Therefore, we have chosen VLA L-band data such that we can get a resolution of $\sim 18''$. This is typically obtained from data with C array. Therefore, we have made images with either C array, C & D array, or if C array data is not available then from D and B array. Data analysis were done using Aips following the standard technique of flagging bad data, calibration using a secondary calibrator, self-calibration and imaging. Details of the data and images obtained are provided in Table-2 along with distances, position and inclination angles of the galaxies. Rms noise of NGC 4490 image made from VLA 1.4 GHz continuum data was significantly higher than expected. Therefore, we used another data set (with the same project code) of bandwidth 6 MHz towards the same object which had long observing time of about 5 hours. We analysed this line data set separately to calibrate and extract the HI line free channels (36 out of 63 channels were used). A continuum image was then made from the line free channels and the rms noise achieved was very close to theoretical expectation. The two continuum images (one from the continuum data with 50 MHz bandwidth and another from the 6 MHz wide line data) were then averaged to get a better 1.4 GHz image of this object with rms noise of $100 \mu\text{Jy}/\text{beam}$. We have also used archival 4.8 GHz images of NGC 3627 (Chyży et al. 2000), 4449 (Soida et al. 2001) and 6 GHz “ uv -tapered ver-

Table 1. Observation at 0.33 GHz with GMRT

| Source name | Observing date | On-source time (hours) | Bandwidth (MHz) | No. of antennas working | Resolution ("×") | Rms (μ Jy/beam) |
|-------------|----------------|---------------------------|--------------------|----------------------------|---------------------|-------------------------|
| NGC 2683 | 11 Jan 2016 | 5.5 | 32 | 29 | 9.5×7.2 | 130 |
| NGC 3627 | 14 Mar 2016 | 3.5 | 32 | 29 | 13.2×8.5 | 450 |
| NGC 4096 | 14 Mar 2016 | 3 | 32 | 29 | 10.8×8.1 | 60 |
| NGC 4449 | 13 Mar 2016 | 4 | 32 | 29 | 10.6×8.2 | 80 |
| NGC 4490 | 13 Mar 2016 | 4 | 32 | 29 | 10.3×7.4 | 70 |
| NGC 4826 | 08 Jan 2016 | 4 | 32 | 28 | 9.2×7.4 | 170 |
| NGC 5194 | 08 Jan 2016 | 4 | 32 | 28 | 9.5×7.8 | 100 |

sion" (Wiegert et al. 2015) of NGC 2683 and 4096 to obtain and study non-thermal spectral indices and CRE propagation in these galaxies.

3.3 Separating thermal emission from radio maps

Typical contribution of thermal emission is about 10% at 1.4 GHz and <5% at 0.33 GHz (Basu et al. 2012b). However, this fraction could be ~20-30% at 1.4 GHz in high star forming regions. Therefore, to study the properties of non-thermal emission from CRes, separation of thermal emission is needed from the radio band maps. H α is a direct tracer of ionised gas density. However, H α emission is attenuated by dust and hence H α maps needs to be extinction corrected. Since the density of dust could be estimated from their IR emission and correction can be made using this feature. Dust absorption corrected H α emission has been used to estimate the thermal emission in the past (Tabatabaei et al. 2007b; Basu et al. 2012b). We use a similar technique as in Tabatabaei et al. (2007b), where they have estimated typical error in modelling the thermal emission could be ~20%. While analysing images from different bands we have converted all images to a common resolution and pixel size.

We have used H α maps for six galaxies, NGC 2683, NGC 3627, NGC 4096, NGC 4449, NGC 4490, NGC 4826 from 11HUGS (Kennicutt et al. 2008). For NGC 5194, H α map from Sings survey (Kennicutt et al. 2003) was used. H α maps have a resolution of $0.3''$ and flux density is recorded in counts. To determine thermal emission, we have converted the unit of those maps from counts to erg/s/cm². Tabatabaei et al. (2007b) used 70 and 160 μ m FIR emission to correct for the dust extinction. We have used the same method using high resolution Herschel maps for the galaxies NGC 3627 (Kennicutt et al. 2011), NGC 4449 (Madden et al. 2013; Karczewski et al. 2013) and NGC 4826 (Kennicutt et al. 2011) at 70 and 160 μ m. We could make thermal maps of these galaxies at the resolution of radio images using H α as a tracer. Herschel data at all the above bands are not available for rest of the galaxies. We have used H α emission along with 24 μ m emission (see below) to model the thermal emission from NGC 2683, NGC 4096 and NGC 4490. We have used Spitzer MIPS 70 μ m (resolution $18''$) and 160 μ m (resolution $40''$) maps (Dale et al. 2009) to model their thermal emission. However, the resolution of these maps were limited to $40''$ as set by the 160 μ m MIPS maps. As described below, we used 24 μ m as a tracer of thermal emission to model them at the resolution of radio images.

We estimated thermal emission from MIPS 24 μ m maps (resolution $6''$) (Rubin 1968; Murphy et al. 2006) following the equation $\frac{S_{\nu,th}}{J_{y,beam}^{-1}} \sim 7.93 \times 10^{-3} T_{e4}^{0.45} \nu_{GHz}^{-0.1} [\frac{f_{24\mu m}}{J_{y,beam}^{-1}}]$. Here T_{e4} is the electron temperature in the unit of 10^4 K, ν_{GHz} is the radio frequency in GHz and $f_{24\mu m}$ is the flux density at 24 μ m. As this emission is not a primary tracer of thermal emission, we have measured the galaxy averaged ratio of thermal emission from H α as a tracer (see above) and from 24 μ m for NGC 2683, NGC 4096, NGC 4490 and NGC 5194. This ratio (correction factor) is expected to depend on the galaxy type and is assumed to not vary within a galaxy. Therefore, we have used the thermal maps from 24 μ m which is multiplied by the correction factor. This allowed us to achieve a resolution comparable to radio maps.

3.4 Non-thermal spectral indices of the sample galaxies

To make spectral index maps from available radio data, we aimed to maximise signal to noise ratio. With certain noises in images made at two different radio frequencies, error in spectrum is minimised if the two frequencies used are far apart. Therefore, if sensitive images of the galaxies with the necessary short spacing in uv distance such that the Fourier transform of the Clean-components from our P-band images show the missing flux density at the typical short spacing ($\sim 500\lambda$ corresponding to shortest spacing of 35m between the antennas in D array) of VLA in C-band is within about 20%, we used thermal subtracted images of that band and P band (~ 0.33 GHz) to make their non-thermal spectral index maps. Available C-band maps of NGC 2683 and 4096 (Wiegert et al. 2015) satisfied the above criteria. C-band images of NGC 3627 (Chyży et al. 2000) and 4449 (Soida et al. 2001) incorporated single dish data and did not suffer from missing flux densities at short uv distances. We used the "uv-tapered version" (Wiegert et al. 2015) of NGC 2683 and 4096. We used the thermal subtracted maps of the above four galaxies to make their non-thermal spectral index maps. For the rest of the galaxies NGC 4490, 4826 and 5194 we used thermal subtracted 1.4 GHz VLA images made for the above. (Non-thermal spectral index images of NGC 2683, 3627, 4096 and 4449 between 1.4 and 0.33 GHz and their thermal emission subtracted 1.4 GHz maps are provided in Supplementary part of this work.) To get the galaxy structures represented adequately in both the frequency maps, we made additional sets of images from the 0.33 GHz GMRT data matching the resolution of the corresponding higher frequency images. Typical UV-coverage obtained within up-

Table 2. Basic properties of the 0.33 and 1.4 GHz images

| Source name | UV range k λ | Resolution ("' \times "') | GMRT Map rms (0.33 GHz) (μ Jy/beam) | VLA Map rms (1.4 GHz) (μ Jy/beam) | VLA Project (1.4 GHz) | Distance of galaxies (Mpc) | Position angle (deg) | Inclination angle (deg) |
|-------------|-------------------------|--------------------------------|--|--|--------------------------|----------------------------------|----------------------------|-------------------------------|
| NGC 2683 | 0.19 – 15 | 19 \times 13 | 200 | 40 | AI23 | 7.7 | 43 | 83 |
| NGC 3627 | 0.26 – 25 | 16 \times 11 | 800 | 370 | AS541 & AP462 | 10. | 170 | 65 |
| NGC 4096 | 0.14 – 17 | 14 \times 12 | 100 | 25 | 16A-013 | 8.3 | 20 | 76 |
| NGC 4449 | 0.15 – 15 | 26 \times 15 | 300 | 180 | AB167 | 4.2 | 0 | 0 |
| NGC 4490 | 0.13 – 14 | 19 \times 18 | 230 | 100 | AA181 | 8.0 | 126 | 60 |
| NGC 4826 | 0.22 – 20 | 15 \times 14 | 280 | 70 | AS541 | 7.5 | 120 | 60 |
| NGC 5194 | 0.15 – 10 | 23 \times 18 | 310 | 30 | AB505 & AN57 | 8.0 | 10 | 20 |

per cutoff of 1.5 $k\lambda$ which provides the structure and intensity distribution of extended emission of sizes of several arc-minutes have been shown for the source NGC 2683 at P-band with GMRT.

4 RESULTS:

We first present the images and spatially resolved spectral index maps of the individual galaxies below and then study the cosmic ray propagation in these galaxies. Radio images made from GMRT 0.33 GHz data of the seven galaxies have been used to generate contour plots (Table-1). As 24 μm emission is a good tracer of thermal emission, we have overlaid in gray scale the corresponding images of the galaxies in IR at an wavelength of 24 μm as observed by Spitzer. These images have been presented below in Figs. 2 to 8. Unless mentioned separately, the lowest contour plotted is 3 times the rms in all the plots presented in this work. We have shown spatially resolved spectral index maps of the galaxies in colour, where we have overlaid in contour the higher frequency continuum images of the corresponding galaxies. For comparison, GMRT 0.33 GHz maps of the galaxies at the same resolution are also presented. These images have been presented below in Figs. 9 to 22. In spectral index maps, pixels for which the signal to noise ratio was less than 5 were blanked. The absolute calibration error for GMRT 0.33 GHz data is typically about 10%, while for the higher frequency data it is believed to be within 2–3%.

4.1 Study of the individual galaxies

(i) NGC 2683: It is a Sb type galaxy seen almost edge-on. This galaxy was observed earlier at 5 GHz (Sramek 1975), and its integrated flux density was measured to be 80 ± 20 mJy. Arecibo observations at 0.43 and 0.61 GHz yielded its flux density as 0.34 Jy (Lang & Terzian 1969). More recent observations with JVLA have shown its flux density to be 66.6 ± 6.5 and 20.3 ± 0.8 mJy at 19 and 5 cm respectively (Wiegert et al. 2015). The resultant galaxy integrated spectral index is -0.9 . The flux densities measured earlier by single dishes could have been affected by confusion and other sources in the field. Total flux density measured from our 0.33 GHz observation is 188 ± 10 mJy, and from the image made from archival VLA C-array data at 1.4 GHz is 56 ± 3 mJy. Galaxy integrated spectrum is -0.84 ± 0.08 , which compares well with the spectrum determined from recent observations at 4.8 and 1.4 GHz. Spectrum of the central core

(-0.4 ± 0.02) and the galactic plane ($\simeq 0.4 - 0.5$) is significantly flatter (Fig. 9) than the out of plane emission of the galaxy.

(ii) NGC 3627: It has a highly prominent bar with wide open arms (galaxy type SAB) and is a member of the Leo group (Dumas et al. 2007). This galaxy has been observed before at 0.327 GHz with VLA with a resolution of $21.0'' \times 16.6''$ (Paladino et al. 2009) and achieved an rms noise of 2 mJy. We have achieved an rms noise of 0.8 mJy/beam, with a beam size of $16'' \times 11''$ at 0.33 GHz. The measured flux density from our 0.33 GHz map is 1.7 ± 0.1 Jy, which is almost double of 0.97 ± 0.03 Jy measured by them. We note that there is a diffuse halo of size of about $6'$ seen around this galaxy, and the flux density for this object includes its contribution. It is likely that due to a higher rms noise of the previous observation, the diffuse extended emission was not seen, which could partly explain the discrepancy. The L-band flux density from the archival VLA data is 0.33 ± 0.01 Jy, which is consistent with what is presented by Paladino et al. (2009). No significant diffuse emission could be seen around this object in L-band map generated from B+D array VLA archival data. They have tabulated its measured total flux densities from 57 MHz to 4.8 GHz and plotted its integrated spectrum. Galaxy integrated spectrum from our measurements at 1.4 and 0.33 GHz is -1.1 ± 0.07 , which is way steeper than what is estimated by them. It is likely caused by the contribution of the halo seen at 0.33 GHz. The spectrum of the central compact emission (-0.48 ± 0.03) and the smaller sized source at the end of the southern bar (-0.59 ± 0.02) is flatter than the rest of the galaxy (see Fig. 11).

(iii) NGC 4096: It is a SABc type galaxy seen almost edge-on. Its flux density measured by Condon (1987) at 20 cm was 52.2 mJy. More recent observations with JVLA have shown its flux density to be 57.1 ± 1.1 and 16.3 ± 0.3 mJy at 19 and 5 cm respectively (Wiegert et al. 2015). From our analysis, measured flux density for this galaxy is 174 ± 10 and 56.2 ± 1.5 mJy from 0.33 GHz GMRT and 1.4 GHz JVLA archival data respectively. Galaxy integrated spectrum is -0.78 ± 0.06 between 1.4 and 0.33 GHz. Emission from the central region has a spectral index of -0.64 ± 0.02 , while that of the Northern compact source (Fig. 4) in the plane of the galaxy is -0.5 ± 0.02 (Fig. 13). Their spectrum is flatter than rest of the galaxy, indicating association of star forming regions with these discrete emissions.

(iv) NGC 4449 is a dwarf irregular Magellanic type of galaxy. Three dense star forming regions can be seen in its 24 μm image (gray) overlaid on the radio map. There is an extended halo seen in both IR and radio maps (Fig. 5). The

SNR 4449-1 is seen as a compact source embedded within the extended halo of the galaxy towards North. Flux density of the galaxy in L-band was measured to be 266 mJy (Condon 1987). It has also been observed with GMRT at 0.61, 0.325 and 0.150 GHz (Srivastava et al. 2014). Their measured flux density for this galaxy at 0.33 GHz is 785 ± 225 mJy, with an rms noise of 1.9 mJy. Our measured flux densities for this galaxy are 517 ± 26 and 259 ± 10 mJy from 0.33 GHz GMRT image and the image made from VLA 1.4 GHz archival data respectively. The rms noise achieved from our 0.33 GHz data after convolving to the archival L-band map is 0.3 mJy/beam (beam size of $26'' \times 15''$), which is ~ 5 lower than the previous observation at 0.33 GHz. This yields galaxy integrated spectrum of -0.48 ± 0.06 between 1.4 and 0.33 GHz. Spectrum of the three dense star forming regions in the south, north-west and north-east are -0.5 ± 0.03 , -0.25 ± 0.02 and -0.66 ± 0.07 respectively (Fig. 15).

(v) NGC 4490: This is a SBm type of galaxy, seen highly inclined. This galaxy was observed in L-band using VLA (Condon 1987), and measured flux density was 774 mJy. This galaxy has also been observed by GMRT at 0.61 GHz by Nikiel-Wroczyński et al. (2016) and measured its total flux density to be 1426 ± 116 mJy. Their measured flux density of this interacting galaxy pair in L-band is 800 ± 41 mJy. Our measured flux densities for this galaxy are 1990 ± 100 and 850 ± 20 mJy from our 0.33 GHz data and 1.4 GHz VLA archival data respectively, which yields galaxy integrated spectrum of -0.59 ± 0.07 . Peak radio emission which appears to be the centre of the galaxy is offset from its peak 24 μm emission (Fig. 6). Significant halo emission is seen in its 0.33 GHz map, which has no counterpart in the 24 μm image, indicating propagation of CRe from the sites of production. It is interacting with its smaller companion NGC 4485 seen towards North West. Its spatially resolved spectral index map (Fig. 17) shows flat spectrum for the emission along its plane. A separate flat spectrum region is also seen to extend from centre towards East (seen along Dec $41^\circ 39'$ from centre), which could be an arm of the galaxy or a region of triggered star formation due to merger of one of its companion galaxy in the past (Lawrence et al. 2020)

(vi) NGC 4826: This is a SAab type of galaxy with medium inclination. This galaxy shows two counter-rotating gas-disks (Braun et al. 1992). This galaxy was observed in L-band using VLA (Condon 1987), and measured flux density to be 103 mJy. Its flux density as measured by Sings survey is 110 ± 10 mJy at 1.365 GHz (Braun et al. 2007). Our measured flux densities for this galaxy are 201 ± 11 and 99 ± 3 mJy from 0.33 GHz GMRT image and the image made from VLA 1.4 GHz archival data. Galaxy integrated spectral index from our measurements is $-0.49 \pm .06$. The central part of the galaxy does show a flatter spectrum of -0.4 ± 0.07 (Fig. 19).

(vii) NGC 5194: This is a Sbc type of grand design spiral galaxy seen nearly face on. It is also interacting with its smaller companion NGC 5195 at its North. This galaxy has been studied extensively in multiple wavebands and was observed as a control sample due to previous observations of this object at 0.33 GHz with GMRT (Mulcahy et al. 2014, 2016). Flux density of this galaxy as measured in L-band is 1490 mJy (Condon 1987). Our measured L-band flux density from the archival C and D array VLA data is 1.2 ± 0.04 Jy. The higher flux density of the earlier L-band image is

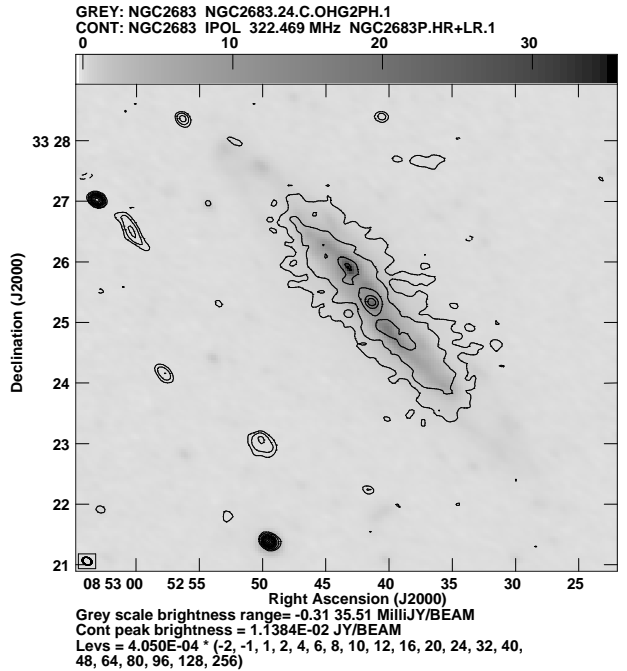


Figure 2. NGC 2683 at 0.33 GHz (contour) and 24 μm (gray). Resolution is $9.5'' \times 7.2''$.

likely due to its value obtained from NRAO single dish map, which is not susceptible to missing zero-spacing problem of an Interferometer. It could also result in part due to a higher confusion noise of single dish measurements. We also compared its flux density from our 0.33 GHz map with the one made earlier from GMRT data using a factor of 2 smaller bandwidth (Mulcahy et al. 2016). Its flux density as estimated by us from the previous GMRT image is 4.8 Jy, while the one imaged by us provides the flux density for the same region as 3.7 ± 0.2 Jy, which is about 30% lower than what is measured from the previous image. This discrepancy could not be due to a calibration error as the flux densities of a few compact source in the field matched within a few percents of each other in the previous map at the same frequency. The difference is also unlikely from missing zero spacing, as our map was made with short UV spacing above 150λ which provides the necessary flux density for the size of NGC 5194 ($\sim 10'$). In fact, the same result was obtained when we did imaging with UV spacing above 100λ . We believe the difference arises from the way the 2 different images have been CLEAN-ed.

4.2 Spectral index

As mentioned in Sect. 1, non-thermal emission has a spectrum close to -0.5 at their origins in star forming regions where thermal fraction is high. Several compact emissions

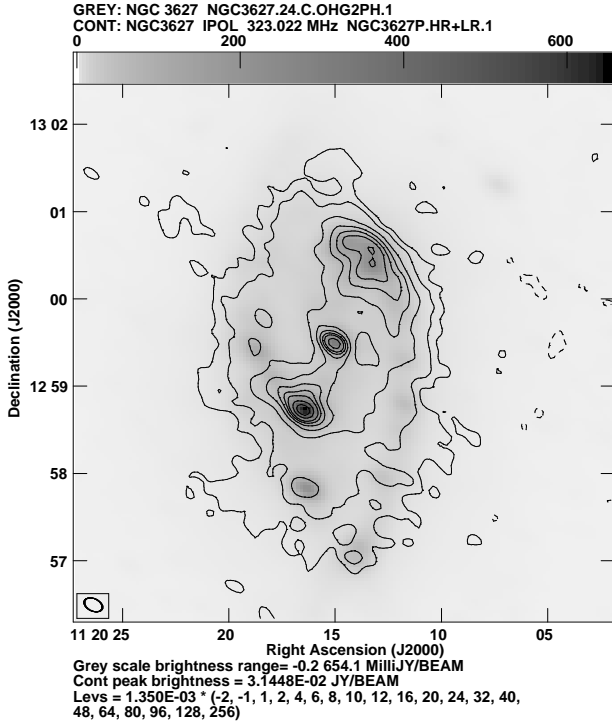


Figure 3. NGC 3627 at 0.33 GHz (contour) and 24 μm (gray). Resolution is $13.2'' \times 8.5''$.

are seen within NGC 2683, 3627 and 4096, and their spectral index maps show these emissions to have flatter spectrum indicating them to be star forming sites. The spectrum of all the galaxies gradually steepens as a function of distance from their centre (where thermal fraction is high) due to propagation loss as they move away to periphery of the galaxies, where thermal fraction is lowest. To investigate this steepening of spectrum from centre to the periphery of the galaxies, we present the azimuthally averaged nonthermal spectrum of the galaxies as a function of galactocentric distance in Figs. 23 to 29. This averaging was performed by the Aips task IRING using the known position and inclination angle of the galaxies, which are also shown in Table-2. We have taken distances of these galaxies from Dale et al. (2009), which are shown in Table-2.

For all the galaxies steepening of the spectrum from the centre to the periphery is observed. It should be noted that star formation happens all across the disk of galaxies (especially in arms of spirals) and radial averaging as done above would average the flatter spectrum of star forming regions at different galactocentric distances with the steeper spectrum of non star-forming region at the same radius (with different position angle).

4.3 Cosmic ray propagation within the galaxies

Mean free path of UV photons (~ 100 pc) that heat the dusts in galaxies is much less than that of CRe at ~ 1 GHz ($\sim 1 - 2$ kpc) (Murphy et al. 2006). CRe are believed to move far away from the source where diffusion plays a significant role (Lerche & Schlickeiser 1982; Ptuskin 2001). If we consider propagation only through diffusion, assume iso-

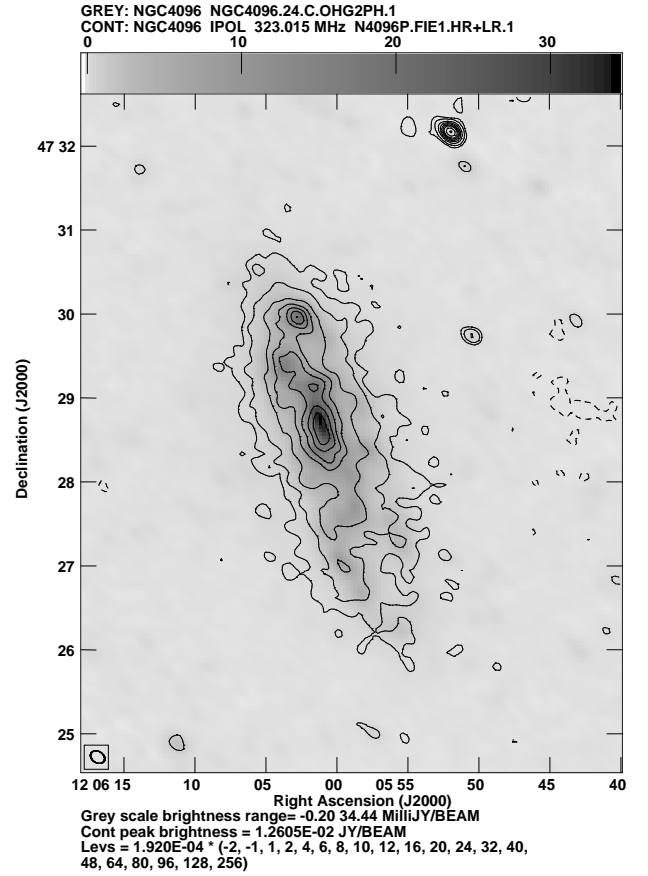


Figure 4. NGC 4096 at 0.33 GHz (contour) and 24 μm (gray). Resolution is $10.8'' \times 8.1''$.

tropic flow of CRe from a compact source, constant spectral index of synchrotron emission and constant magnetic field, then the emission is really dependent on the densities of the CRe as they propagate from the sources. Then as shown in Appendix, after a time (t) from turning-on of a CR source, CRe density would follow a Gaussian distribution with distance from source. FWHM of Gaussian profile is determined by the denominator of the exponential, which is $\sqrt{D\tau\nu}$. The above simple model of CRe diffusion would therefore cause the radio image of a galaxy to appear as a convolution with a Gaussian of its FIR image (consisting of many compact and extended sources). In practice, this would cause smearing of high frequency images of a galaxy in radio band (Bicay & Helou 1990). Considering most of the emission occurs at critical frequency (ν_c), for synchrotron emission at a frequency ν , the half life of synchrotron emission ($T_{(1/2)\nu}$) in a constant magnetic field is $\propto \nu^{-0.5}$. Therefore, ratio of propagation length scales at those two frequencies will be $(\nu_1/\nu_2)^{-1/4}$, which can be tested from our observations. Numerical simulations considering isotropic pitch angle distribution of CRe with power law distribution of energy (Ginzburg & Syrovatskii 1965) having power law index between 2 and 3 show that ratio of emission between time $T = 0$ and after $T_{(1/2)\nu}$ for both the frequencies between 0.33 GHz and 6 GHz remains about the same. As the fall in emission at the two frequencies after respective $T_{(1/2)\nu}$ occur by the same factor, the above estimation of the ratio of

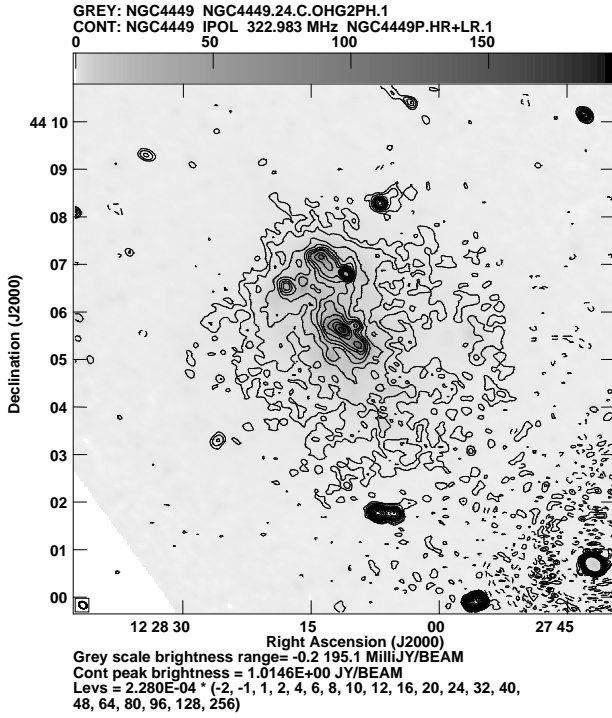


Figure 5. NGC 4449 at 0.33 GHz (contour) and 24 μm (gray).
 Resolution is $10.6'' \times 8.2''$.

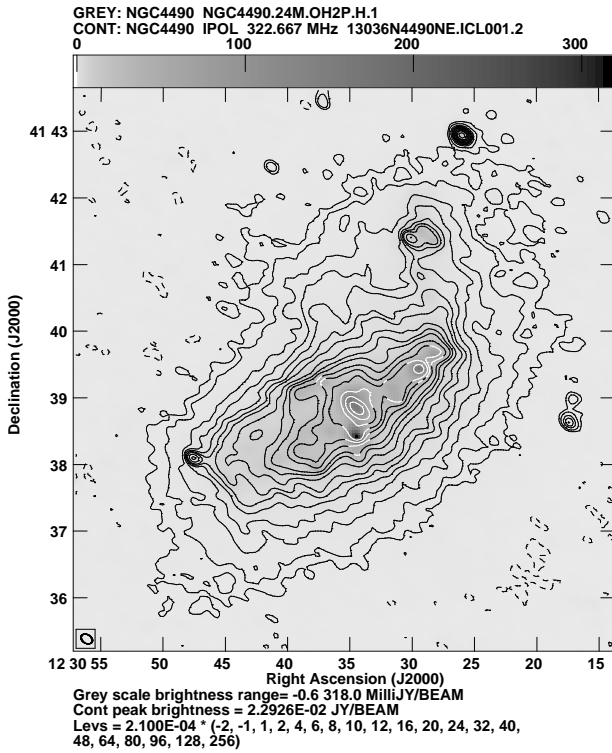


Figure 6. NGC 4490 at 0.33 GHz (contour) and 24 μm (gray).
 Resolution is $10.3'' \times 7.4''$.

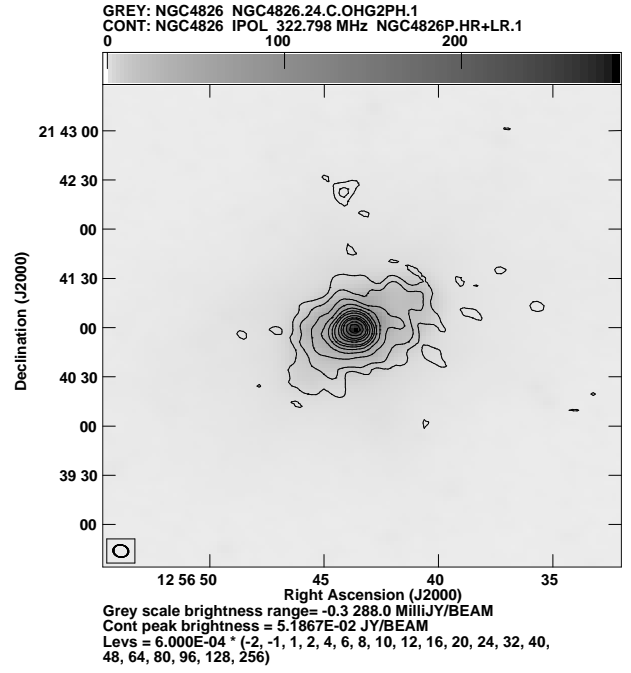


Figure 7. NGC 4826 at 0.33 GHz (contour) and 24 μm (gray).
 Resolution is $9.2'' \times 7.4''$.

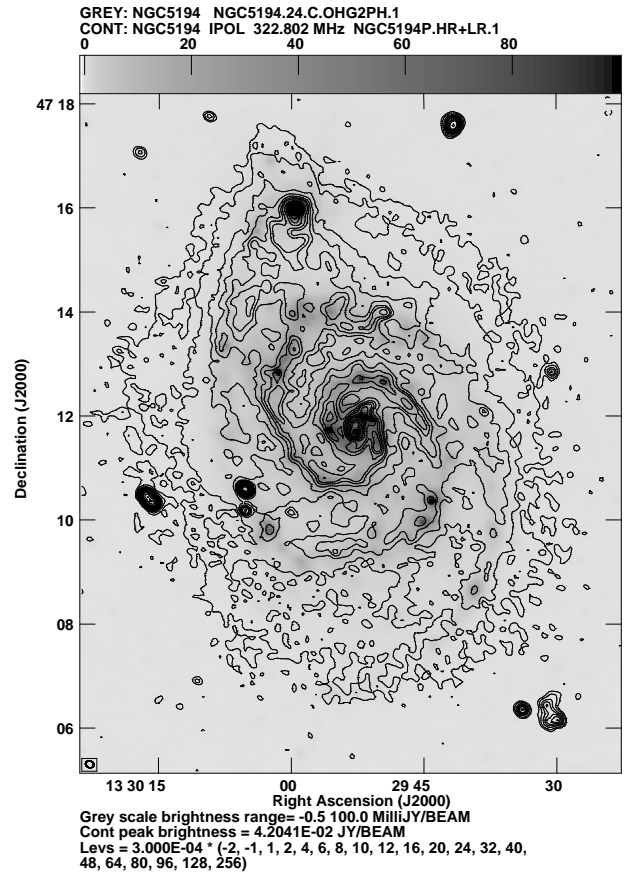


Figure 8. NGC 5194 at 0.33 GHz (contour) and 24 μm (gray).
 Resolution is $9.5'' \times 7.8''$.

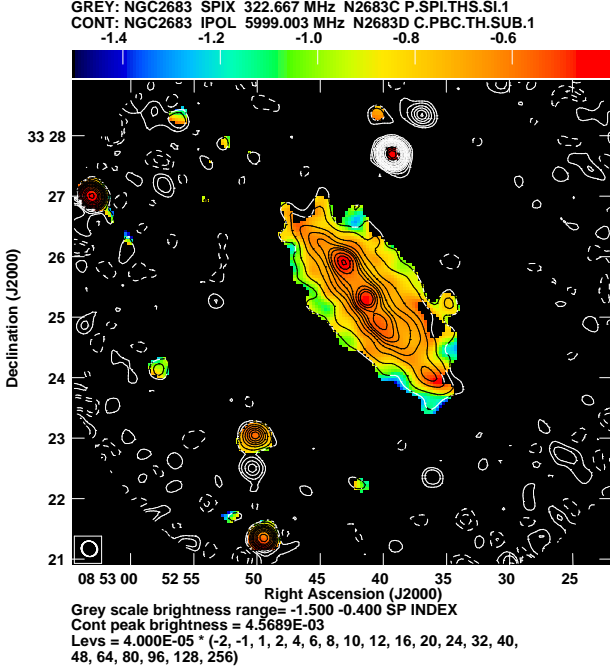


Figure 9. Thermal emission subtracted 6 GHz map (contour) and non-thermal spectral index of NGC 2683 (colour) between 0.33 and 6 GHz. Resolution is $15.9'' \times 14.8''$.

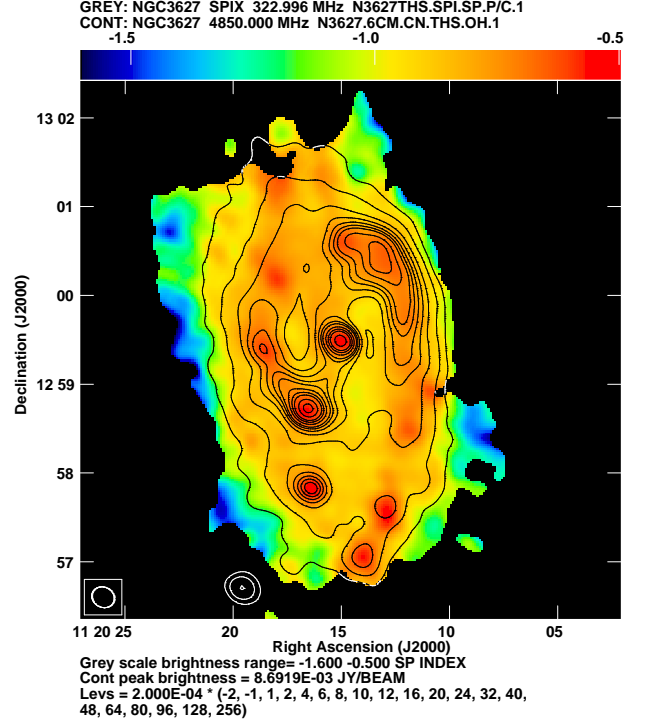


Figure 11. Thermal emission subtracted 5 GHz map (contour) and non-thermal spectral index of NGC 3627 (colour) between 0.33 and 5 GHz. Resolution is $15.7'' \times 13.6''$.

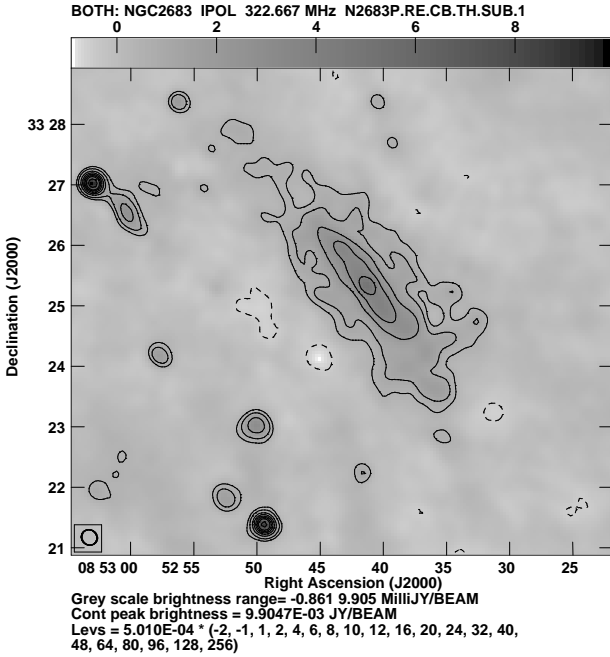


Figure 10. Thermal emission subtracted 0.33 GHz map (in contour & Gray scale) of NGC 2683. Resolution is $15.9'' \times 14.8''$.

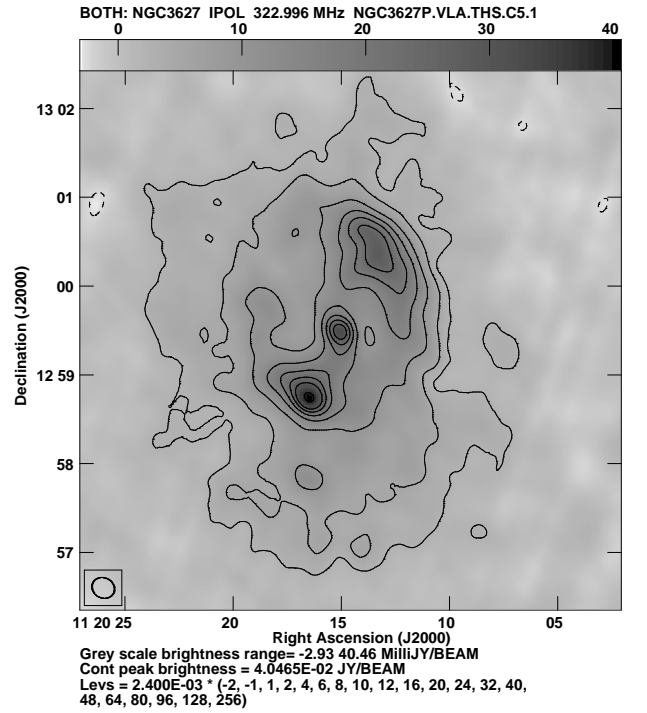


Figure 12. Thermal emission subtracted 0.33 GHz map (in contour & Gray scale) of NGC 3627. Resolution is $15.7'' \times 13.6''$.

propagation scale at two different frequencies remains valid in general. It should be noted that CRs can also propagate through other mechanisms, which include galactic wind, streaming instability (Amato & Blasi 2018) or a combination of the above three mechanisms. Depending on the mechanisms responsible, the ratio of propagation lengths for the

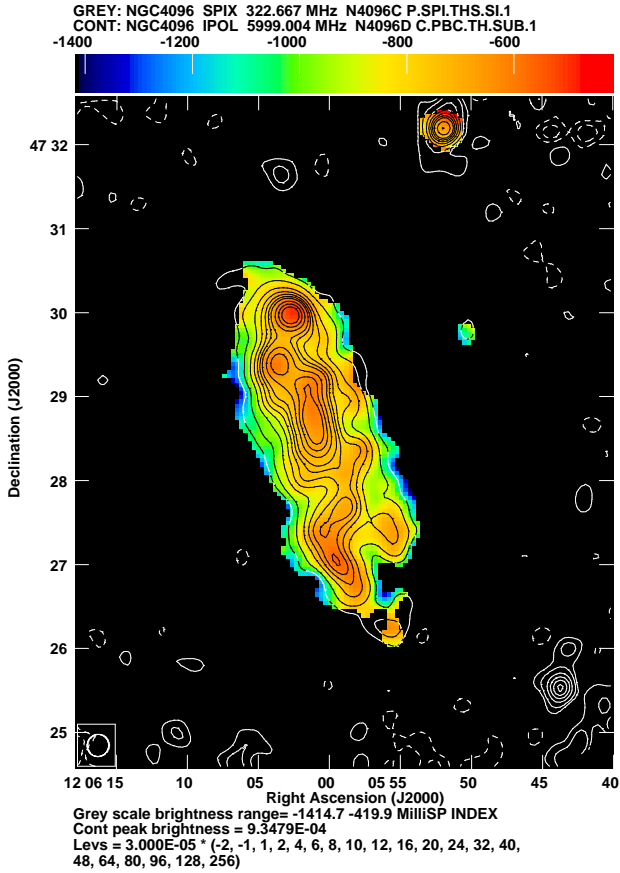


Figure 13. Thermal emission subtracted 6 GHz map (contour) and non-thermal spectral index of NGC 4096 (colour) between 0.33 and 6 GHz. Resolution is $15.9'' \times 15.3''$.

two frequencies would differ. For CRE propagation through galactic wind, the ratio is independent of frequency, and for streaming instability (distance travelled $\propto \tau$) the ratio would be $(\nu_1/\nu_2)^{-1/2}$ (Tabatabaei et al. 2013). In this paper, we investigate whether the above simple model of diffusion is consistent with our observations.

To estimate the propagation distance of the CReS, we assume that the CReS loss energy mostly by synchrotron emission such that the exponent of radio FIR correlation is unity. Within galaxies this can happen when CRE propagation do not play important role as in flat spectrum star forming regions (Heesen et al. 2019). To attain the same from the available maps of the galaxies, we use the method of Berkhuijsen et al. (2013). This method uses convolution by different kernel sizes of the FIR maps of an object till the exponent of radio and convolved FIR map becomes unity. Radio-FIR correlation often uses monochromatic FIR emission at $70 \mu\text{m}$, which we also use for the above purpose. A similar approach has also been used recently by Vollmer et al. (2020) to study CRE propagation mechanism using 6 and 20 cm radio maps of spirals. We convolved the $70 \mu\text{m}$ Spitzer FIR maps of the galaxies with different Gaussian FWHM using Aips task CONVL. The standard radio-FIR correlation of the form

$$S_{\text{radio}} = a.(S_{\text{FIR}})^b \quad (1)$$

was used to determined b for different values of FWHM. In

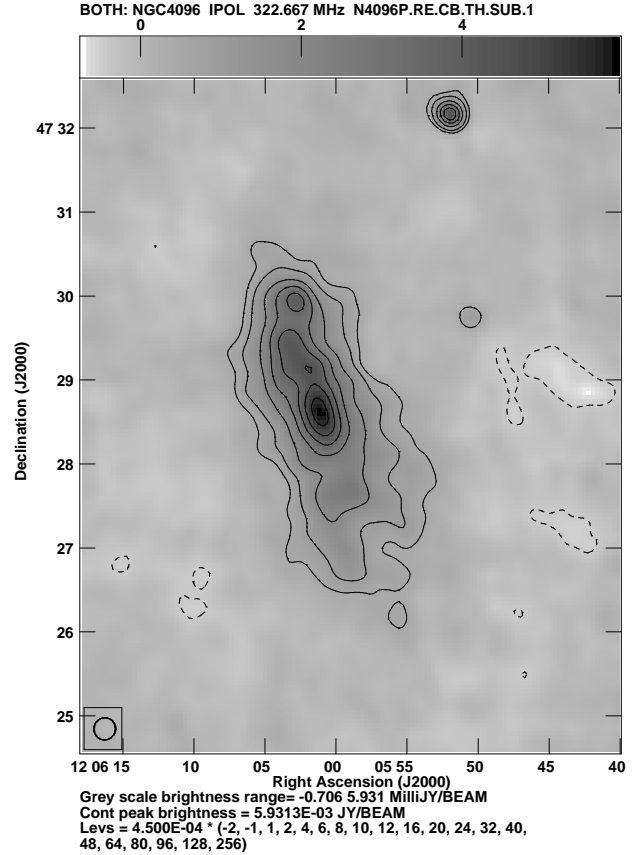


Figure 14. Thermal emission subtracted 0.33 GHz map (in contour & Gray scale) of NGC 4096. Resolution is $15.9'' \times 15.3''$.

practice, we consider the two maps to have matched when the derived value of b is consistent with unity within the fitting error.

Blanking:

Not all the emission regions in the maps of each of the galaxies could be well fitted by unique values of ‘ a ’ and ‘ b ’. In certain cases, this happened when there are compact background radio sources (often AGNs) seen through the galaxies in the maps. In such cases, the regions containing the background sources were blanked from the corresponding radio map. This approach was needed for NGC 5194, where 4 background sources in the field were blanked. Moreover, for this field, the part of the map showing the interacting galaxy NGC 5195 was blanked. The central region of the galaxy is very bright in radio suggesting contribution from the central AGN. Therefore, we have blanked the central small diameter source from the FIR map of NGC 5194. NGC 4449 is a dwarf irregular type of galaxy and has three distinct dense star forming regions (Fig. 5). Two of these compact regions in its north show different exponents in the radio-FIR maps than the rest of the galaxy. Therefore, to remove contribution from the two star forming regions, we blanked them along with their surrounding pixels (within a couple of beam-widths). The only other galaxy that required blanking was NGC 4490. As it is interacting with its smaller companion NGC 4485 towards its North-East, the part containing the companion and the bridge of emission joining it was

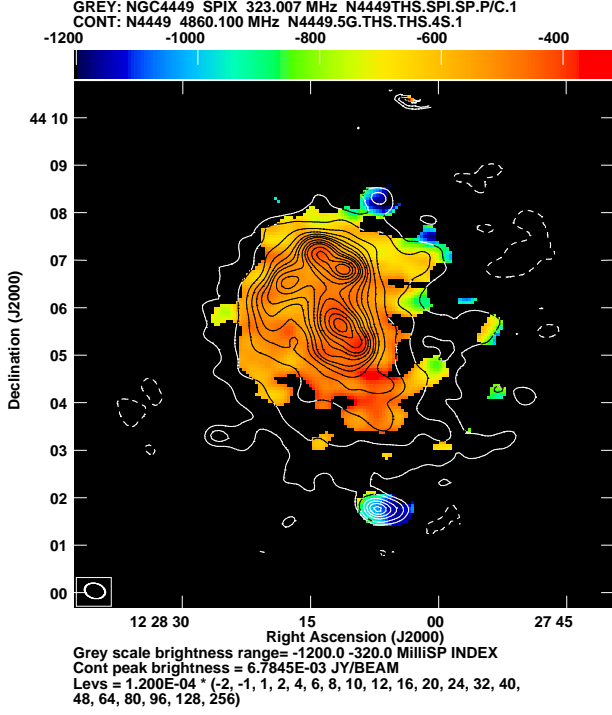


Figure 15. Thermal emission subtracted 5 GHz map (contour) and non-thermal spectral index of NGC 4449 (colour) between 0.33 and 5 GHz. Resolution is $26.1'' \times 19.1''$.

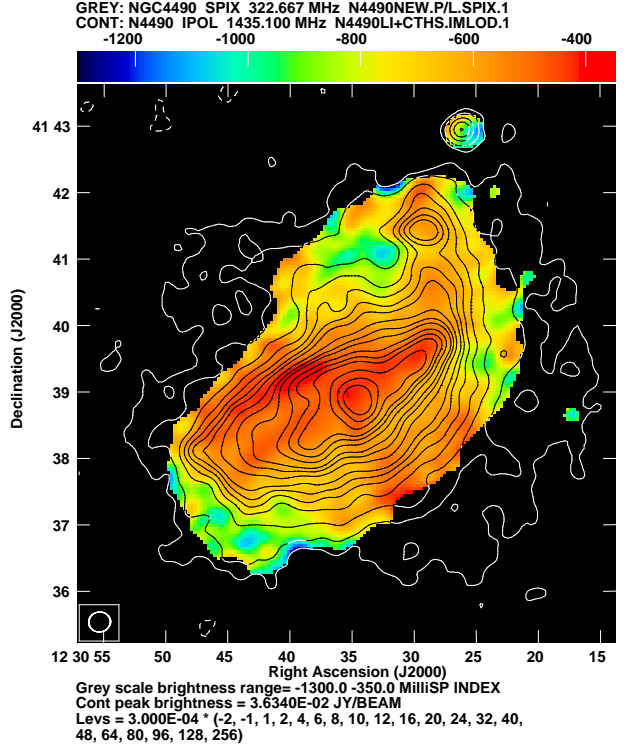


Figure 17. Thermal emission subtracted 1.4 GHz image (contour) and non-thermal spectral index of NGC 4490 (colour) between 0.33 and 1.4 GHz. Resolution is $19'' \times 18''$.

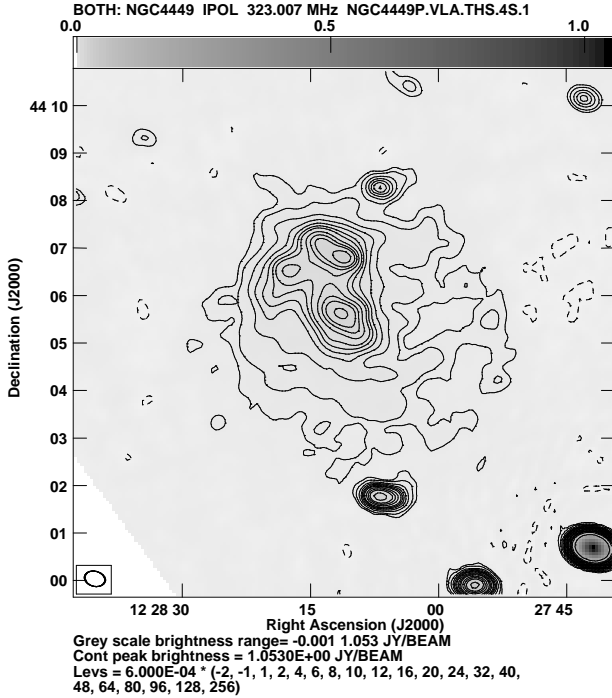


Figure 16. Thermal emission subtracted 0.33 GHz map (in contour & Gray scale) of NGC 4449. Resolution is $26.1'' \times 19.1''$.

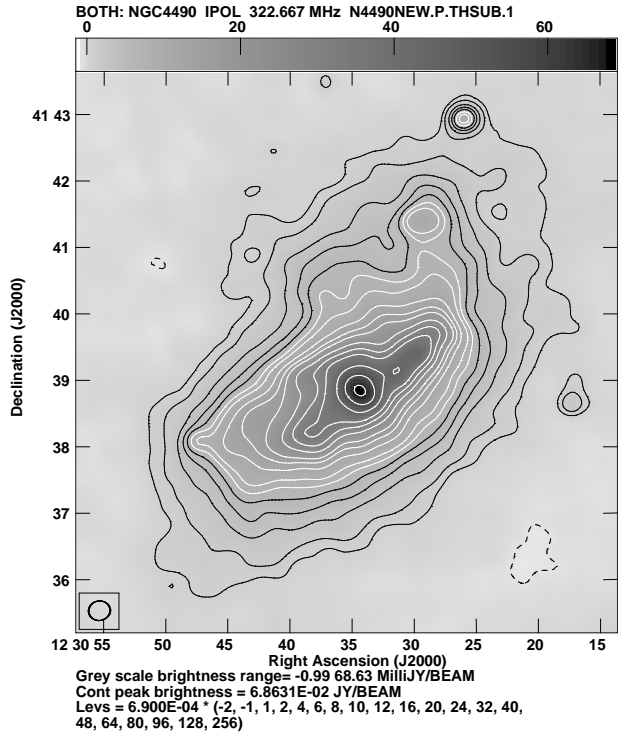


Figure 18. Thermal emission subtracted 0.33 GHz map (in contour & Gray scale) of NGC 4490. Resolution is $19'' \times 18''$.

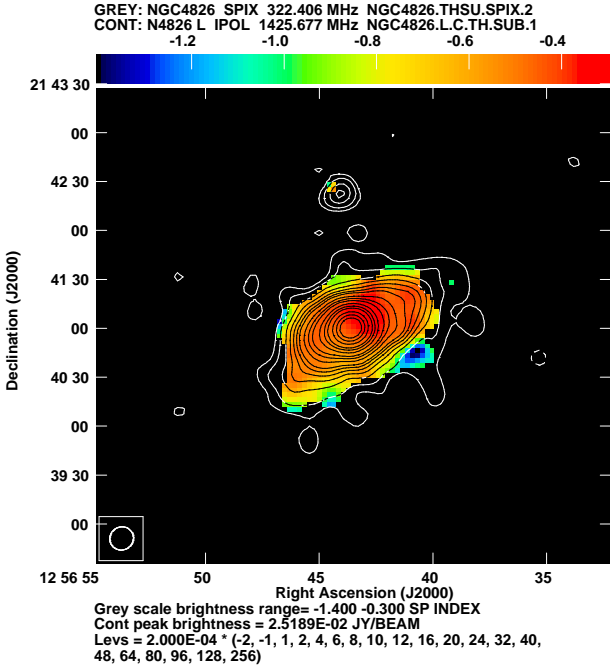


Figure 19. Thermal emission subtracted 1.4 GHz image (contour) and non-thermal spectral index of NGC 4826 (colour) between 0.33 and 1.4 GHz. Resolution is $15'' \times 14''$.

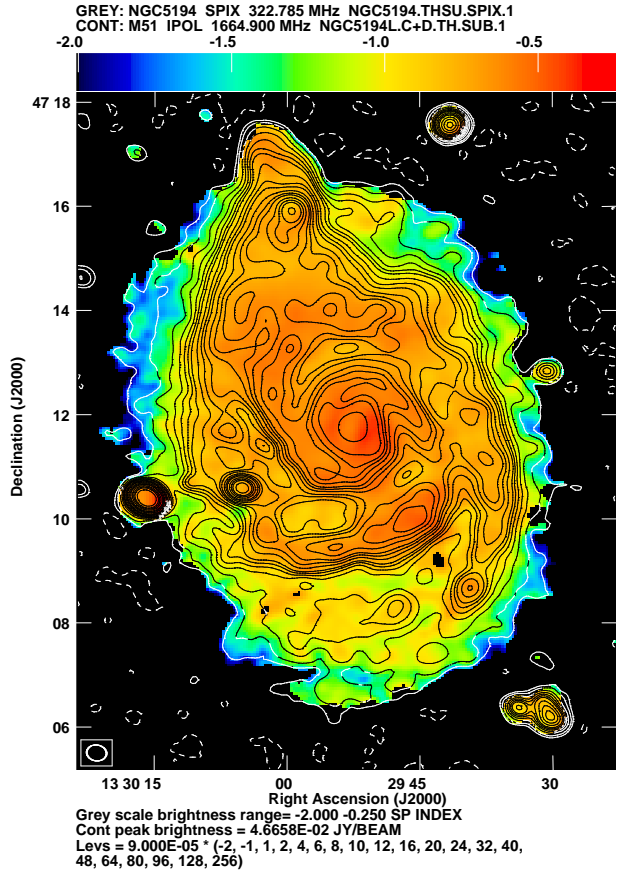


Figure 21. Thermal emission subtracted 1.4 GHz image (contour) and non-thermal spectral index of NGC 5194 (colour) between 0.33 and 1.4 GHz. Resolution is $23'' \times 18''$.

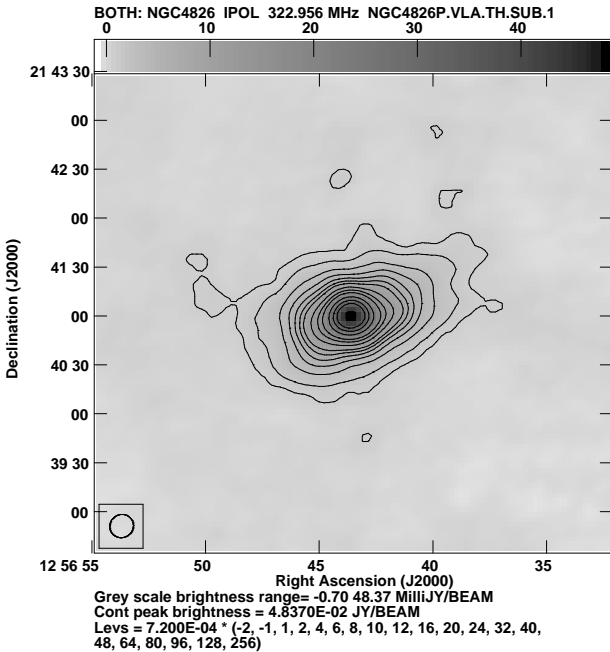


Figure 20. Thermal emission subtracted 0.33 GHz map (in contour & Gray scale) of NGC 4826. Resolution is $15'' \times 14''$.

blanked.

Correlation of the convolved FIR maps with radio:

To get a reasonable fit of equation (1) to the pixel values of the above maps, we have chosen cutoff in radio intensities of $\sim 2 - 5$ times than the corresponding map rms. (We have set the lower cutoff high to better reject noisy data. However,

to get a fit over a large fraction of data for certain galaxies with poorer signal to noise ratio, the cutoff was brought down up to 2σ). In the radio-FIR plots, multiple radio flux densities (along y-axis) do occur within very close range of FIR (along x-axis). Removing lower values along y-axis for a particular point along x-axis would bias the fit. Therefore, when cut-offs along y-axis were applied, we also applied a corresponding lower cut-off along x-axis such that most of the y-axis points below the threshold gets excluded from the fit due to cut along x-axis. Near the highest flux densities in the plots, systematic deviations were noted for several galaxies. In such cases, upper cutoffs were also applied while ensuring that it does not cause rejection of more than a few percent of the total pixels. The fitted values of convolution FWHM corresponding to 0.33, 1.4 and ~ 6 GHz maps are shown in Table-3.

The following procedure was used to estimate FWHM of the convolving Gaussian. We initially convolved the $70\ \mu\text{m}$ map of each galaxy with FWHM of $1'$, $2'$ and $3'$ and compared the 'b' values for the three different propagation ranges. Depending on these comparisons we further fine-tuned FWHM of the kernels so that 'b' reaches unity for 0.33, 1.4 and ~ 5 GHz maps. The fits for each of the galaxies are described below.

(i) NGC 2683: For this galaxy, the lower cutoff for the fit to the 0.33 GHz radio data was 0.4 mJy/beam (2σ). For

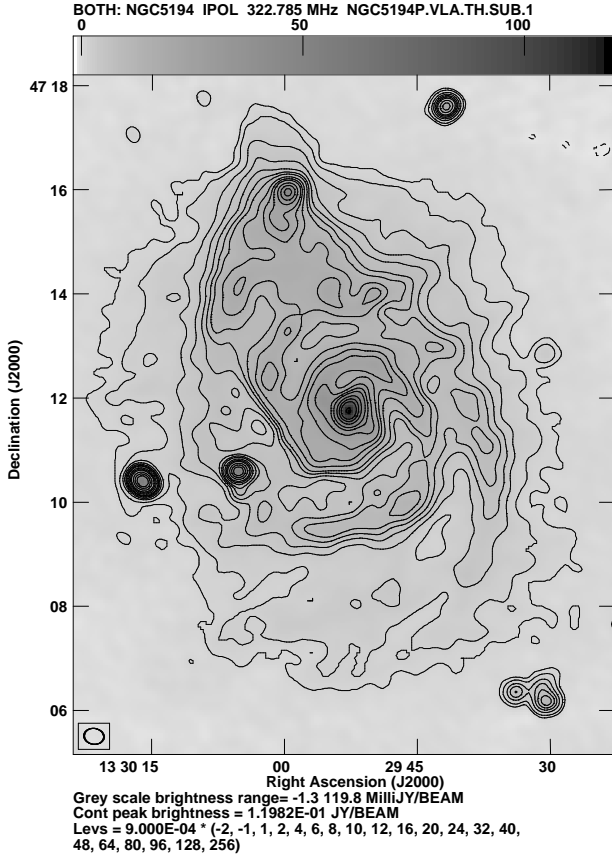


Figure 22. Thermal emission subtracted 0.33 GHz map (in contour & Gray scale) of NGC 5194. Resolution is $23'' \times 18''$.

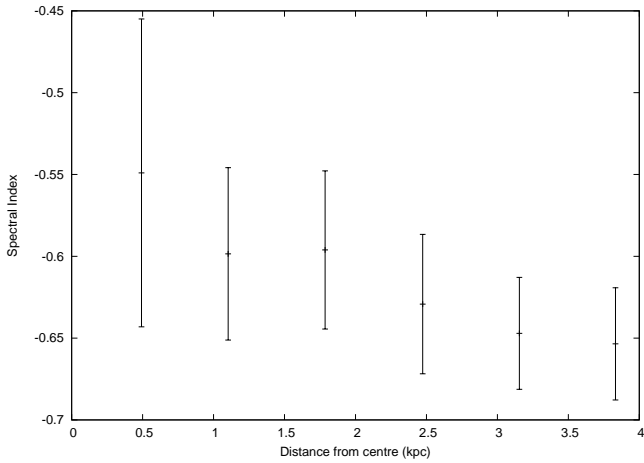


Figure 23. Radial variation of non-thermal spectral index for NGC 2683.

the reasons described above, FIR range for the fit was 3 to 6.8 Jy/beam. Convolution with Gaussian FWHM of $115''$ produced correlation of 0.93 with 0.33 GHz radio map, with $db/d\theta = 0.3 \text{ arc-min}^{-1}$. Gaussian convolution FWHM for $b = 1$ with the 330 MHz map is $130'' \pm 24''$. With radio map at 1.4 GHz, the lower limit of the radio flux density was 0.2 mJy/beam, and FIR range between 0.3 to 1.7 Jy/beam. The size of Gaussian FWHM for b to be unity was $21'' \pm 8''$. With

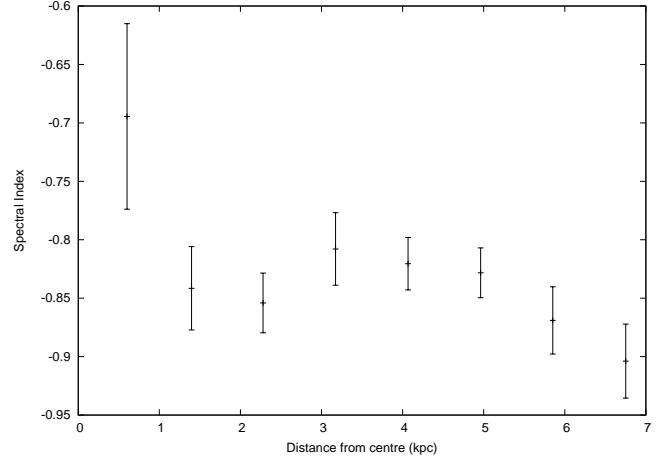


Figure 24. Radial variation of non-thermal spectral index for NGC 3627.

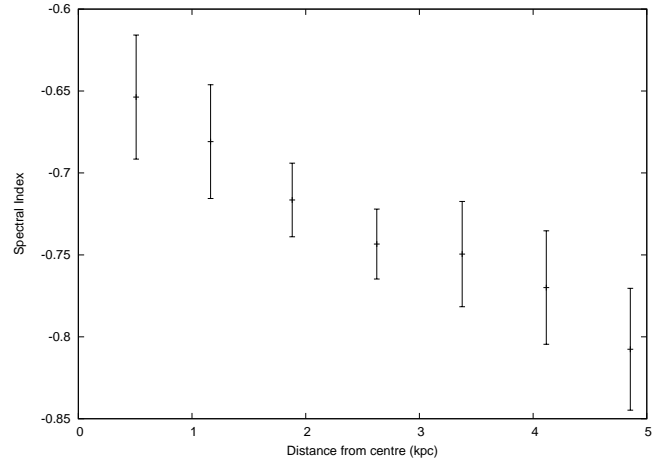


Figure 25. Radial variation of non-thermal spectral index for NGC 4096.

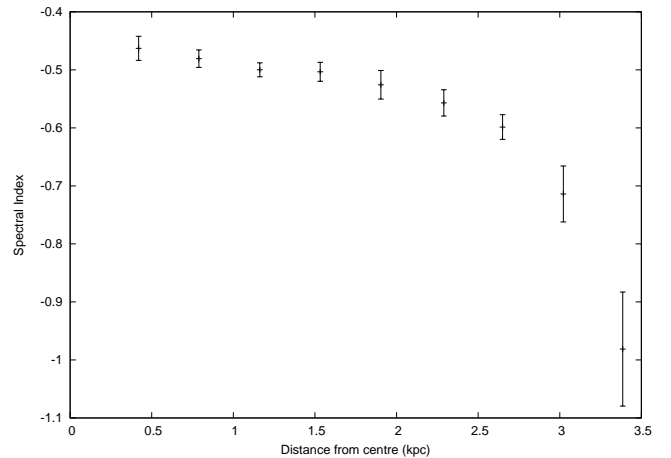


Figure 26. Radial variation of non-thermal spectral index for NGC 4449.

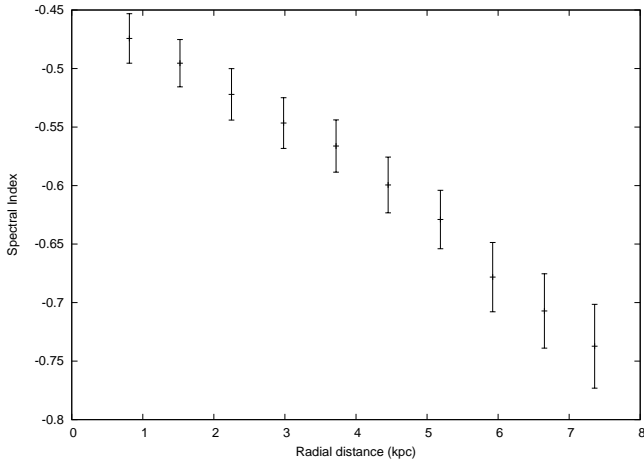


Figure 27. Radial variation of non-thermal spectral index for NGC 4490.

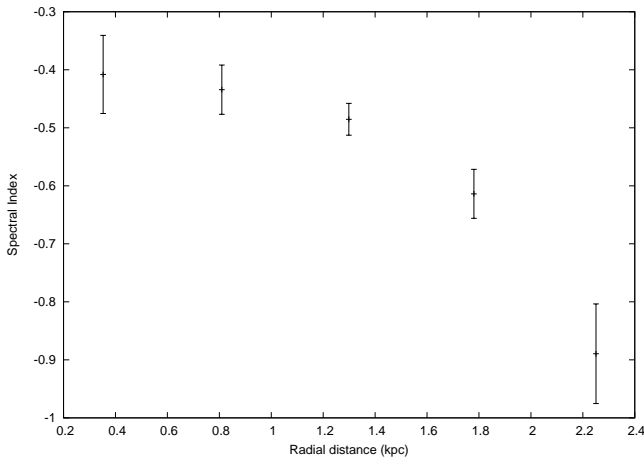


Figure 28. Radial variation of non-thermal spectral index for NGC 4826.

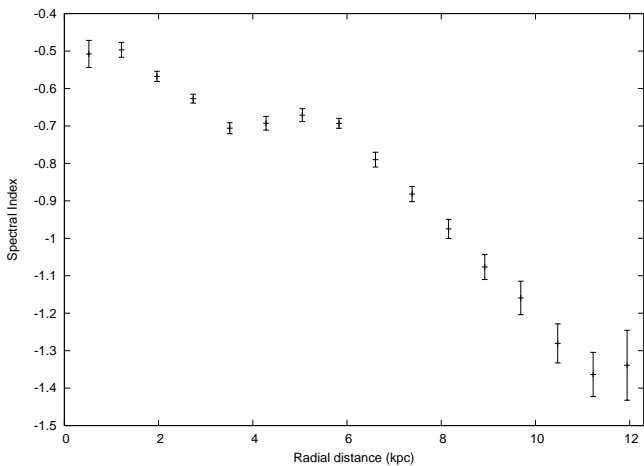


Figure 29. Radial variation of non-thermal spectral index for NGC 5194.

thermal subtracted radio map at 6 GHz, the lower limit of flux density was 0.055 mJy/beam, and FIR range 0.1 to 0.5 Jy/beam. For b to be unity, convolution FWHM is $21'' \pm 7''$.

(ii) NGC 3627: The lower cutoff for the fit to the 0.33 GHz radio data was 3.0 mJy/beam ($\sim 4 - \sigma$). FIR range used for the fit was 7 to 22 Jy/beam. For a FWHM of $120''$, the fitted value of b was 1.0 ± 0.1 . For b to be unity, convolution FWHM is $120'' \pm 24''$. The 1.4 GHz image from VLA archival data has less structural sensitivity than the 0.33 GHz map and we do not see the extended halo seen in the 0.33 GHz map around the arms of the galaxy. Therefore, we do not estimate the CRE propagation FWHM from the 1.4 GHz observations. We used its 4.8 GHz map made by combining single dish Effelsberg image with VLA image (Soida et al. 2001). After subtracting the expected thermal emission, we used a fit limit on FIR data between 1.5 and 8 Jy/beam and radio data above 0.4 mJy/beam. For b to be unity, convolution FWHM is $20'' \pm 4''$.

(iii) NGC 4096: The lower cutoff for the fit to the 0.33 GHz radio data was 0.5 mJy/beam (3σ). FIR limits were 0.5 to 2.5 Jy/beam. With convolving Gaussian FWHM size of $53''$, the fitted value of b was 1.0 ± 0.1 , yielding convolution FWHM of $53'' \pm 15''$. The same for the 1.4 GHz map is $31'' \pm 10''$. Lower limit used for the fit from 1.4 GHz radio was 0.125 mJy/beam and FIR ranges for the fit were 0.15 to 1.7 Jy/beam. With 6 GHz radio map, lower limit of the fit was 0.05 mJy/beam, and FIR limits used were 0.2 to 1.2 Jy/beam. However, there were certain inconsistencies in convolution sizes using the FIR map for b to be unity. We could only get an upper limit on the convolution size of $32''$.

(iv) NGC 4449: With radio data between 0.6 to 5 mJy/beam and a lower limit of 3 Jy/beam in FIR, the derived value of convolution FWHM is $90'' \pm 12''$ for the 0.33 GHz map. The same for the 1.4 GHz map is $115'' \pm 15''$. The lower limit of radio flux density was 0.5 mJy/beam ($\sim 3\sigma$), and to avoid systematic deviation, an upper cutoff of 14 mJy/beam was used. FIR lower limit was 4 Jy/beam. The 1.4 GHz image from VLA archival data has less structural sensitivity than the 0.33 GHz map. Therefore, we used its 4.8 GHz map made by combining single dish Effelsberg data with VLA (Chyży et al. 2000). After subtracting the expected thermal emission, we used a fit limit on FIR data between 1. and 7 Jy/beam and radio data above 0.1 mJy/beam. For b to be unity, convolution FWHM is $62'' \pm 10''$.

(v) NGC 4490: With radio data above 1 mJy/beam and a lower limit of 2.5 to 18 Jy/beam in FIR, the derived value of Gaussian convolution FWHM is $86'' \pm 17''$ for the 0.33 GHz map. The same for the 1.4 GHz map is $55'' \pm 8''$. The lower limit of radio flux densities used for the fit was 0.5 mJy/beam (5σ). To avoid systematic deviation from the fit, FIR range used was 1.0 to 12 Jy/beam.

(vi) NGC 4826: Emission from this galaxy is dominated by the central region, which is not well resolved with an angular resolution of $18''$. Diffuse extended emission is seen around it. The centrally peaked emission is seen in radio and IR (Fig. 7). However, contribution from hidden Active Galactic Nuclei (AGN) at the centre cannot be ruled out for this galaxy in radio band. With 0.33 GHz radio data above 0.34 mJy/beam (4σ) and an FIR lower limit of 0.5 Jy/beam, the value of b using $70 \mu\text{m}$ map without any convolution is greater than unity indicating FIR emission is more diffuse

than radio. Therefore, CRe propagation scale cannot be determined by the above method for this galaxy. Hence, we have kept the Gaussian convolution FWHM blank for this object in Table-3.

(vii) NGC 5194: With radio data between 1.0 and 25 mJy/beam and FIR data above 4 Jy/beam, the derived value of convolving Gaussian is $150'' \pm 10''$ for the 0.33 GHz map. The same for the 1.4 GHz map is $75'' \pm 10''$. The lower and upper limit of radio flux densities used for the fit was 0.2 to 10 mJy/beam. To avoid systematic deviation, a lower cutoff of 0.7 Jy/beam was used for FIR. We also compared the propagation scale at 0.14 GHz from LOFAR map (Mulcahy et al. 2014) after thermal subtraction. With radio data above 1 mJy/beam and FIR data between 8 to 45 Jy/beam, the derived value of FIR convolution size for $b = 1$ is $193 \pm 14''$ (7.8 ± 0.6 kpc). It is a factor of two larger than what is found by Heesen et al. (2019) for this galaxy. They used convolution of hybrid-SFR surface density map to obtain unit exponent for SFR surface density from hybrid-SFR and 1.4 GHz radio. We note that their method uses a combination of FUV and $24 \mu\text{m}$ data to define the star forming disk, while the method used in this work uses $70 \mu\text{m}$ FIR.

4.4 Spatially resolved radio-FIR correlation

Spatially resolved study of radio-FIR correlation has been carried out using 1.4 and 0.33 GHz radio maps and $70 \mu\text{m}$ FIR map. These maps were blanked as described in Sect. 4.3.

Radio-FIR correlations were studied by fitting Equation. 1. Arm and inter-arm region could be isolated in NGC 5194. For other galaxies we could not separate arm and interarm region visually and used the spatially resolved emission across the galaxies for this study. All images were convolved to the same resolution as shown in Table-2 using the task CONVL in Aips. The cut-offs used for the correlation fits in radio are the same as described in Sect. 4.3, where criteria used for FIR ranges are also described. Logarithm (base 10) of FIR ranges (in Jy/beam) used for NGC 2683, 3627, 4096, 4449, 4490, 4826 with 0.33 GHz radio data were -1 to -0.222 , > -1 , -1.3 to -0.22 , > -1 , > -1.33 , and > 0.079 respectively. FIR Ranges used (in dex) with 1.4 GHz radio data for the above galaxies were -0.824 to -0.222 , > 0.079 , -1.398 to -0.22 , > -1 , > -1.22 and > -0.22 respectively. The FIR ranges used for the arm regions of NGC 5194 were > -0.7 and > -1.0 with 0.33 and 1.4 GHz radio data respectively. The above ranges for interarm regions of NGC 5194 were > -0.7 and > -1.3 respectively.

The radio-FIR correlations for all the galaxies are presented in Figs. 30 to 37. In these plots, 0.5 dex has been added to the 0.33 GHz radio data to avoid any overlap with the 1.4 GHz radio data. All the correlation values are given in Table-4. We have also provided the scatter of the correlation which is the rms distance of all points from the fitted line. In all the figures mentioned above, data points for the 1.4 GHz radio appear lower than the 0.33 GHz values. All the plots except for NGC 5194 include all the pixels selected. However, while estimating the errors, we have accounted for the number of pixels in a synthesised beam (resolution), values of which are correlated. For NGC 5194, we could separate arm and interarm regions visually using the Spitzer $24 \mu\text{m}$ map, which we have selected by visual masking, and these plots are shown in Fig. 36 and 37. Exponents for the

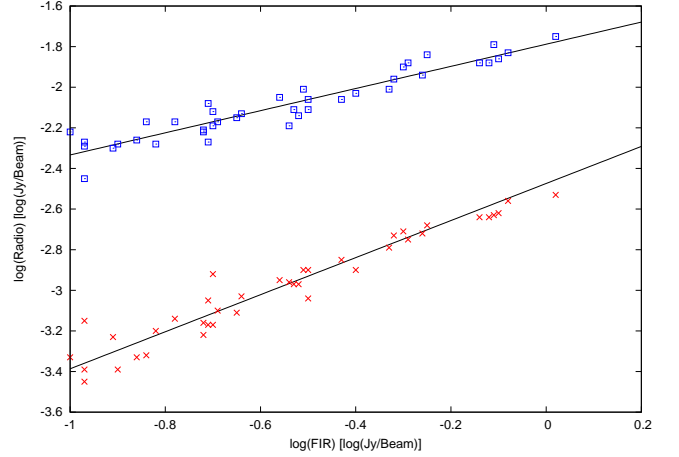


Figure 30. $70 \mu\text{m}$ FIR vs 0.33 and 1.4 GHz radio intensity (lower plot) of NGC 2683. Note: To prevent overlap of 0.33 GHz data with the 1.4 GHz data on the plot, 0.5 dex has been added to the 0.33 GHz data.

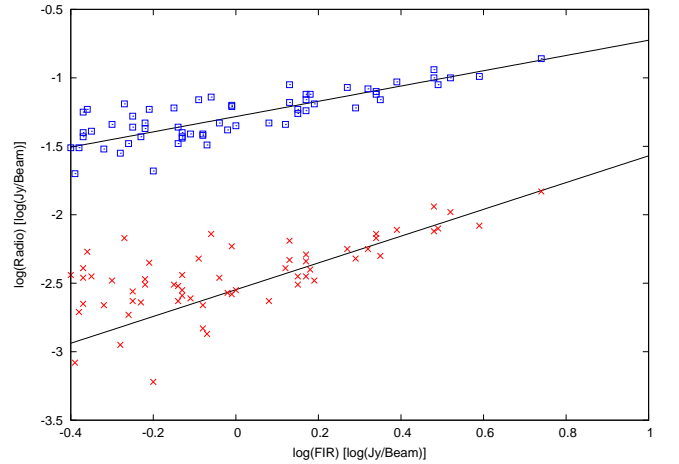


Figure 31. $70 \mu\text{m}$ FIR vs 0.33 and 1.4 GHz radio intensity (lower plot) of NGC 3627. To the 0.33 GHz data 0.5 dex has been added.

0.33 GHz radio and FIR varies from 0.5 to even higher than 1. However, the exponent (b) using 1.4 GHz radio data is always higher than 0.33 GHz data except for NGC 4449. This is consistent with what was found by Basu et al. (2012b).

5 DISCUSSIONS

5.1 How cosmic ray electrons propagate in nearby galaxies

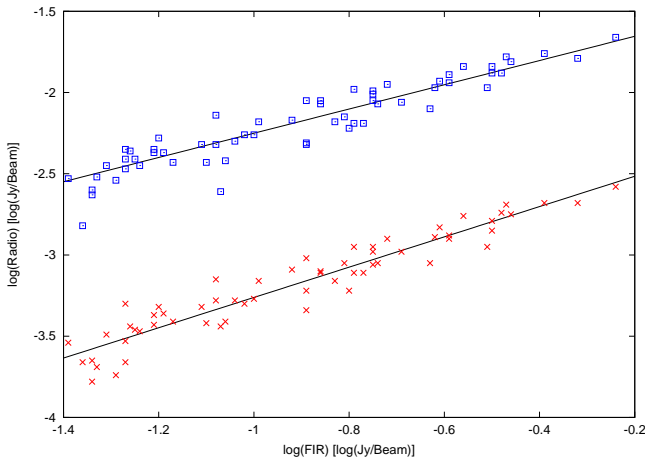
As discussed in Sect. 4.3, CReS are expected to spread out from the sources of emissions in a galaxy. Therefore, compared to FIR band, where the thermal sources of emissions are mostly seen and which are believed to give rise to CReS, radio image of a galaxy would appear to be smeared by a convolution function (kernel). For the simple scenario of CRe diffusion, ratio of FWHMs of these kernels is $\propto (\nu_1/\nu_2)^{-1/4}$. Therefore, the ratio of FWHMs in this case is ~ 1.4 between 0.33 and 1.4 GHz, and ~ 2.1 between 0.33 and ~ 6 GHz. For propagation through streaming instability, the ratio is $\propto (\nu_1/\nu_2)^{-1/2}$, which is ~ 2.1 between 0.33 and 1.4 GHz,

Table 3. Gaussian convolution FWHM derived from radio-FIR correlation for $b = 1$

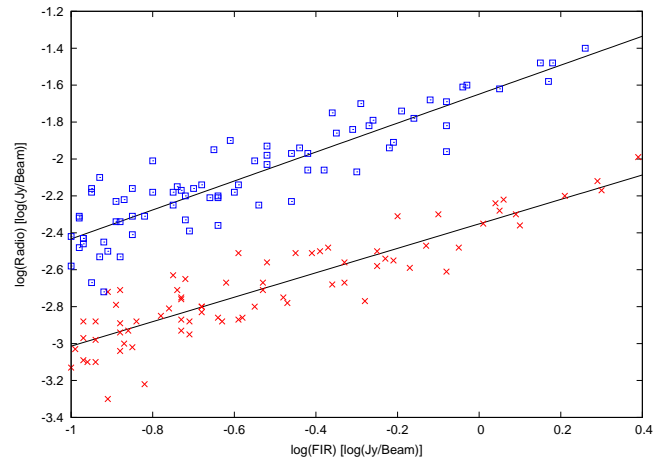
| Galaxy name | FWHM at 0.33 GHz | | FWHM at 1.4 GHz | | FWHM ratio between 0.33 & 1.4 GHz | FWHM at ~ 6 GHz | | FWHM ratio between 0.33 & ~ 6 GHz |
|-------------|------------------|----------------|-----------------|---------------|--------------------------------------|----------------------|---------------|---|
| | arc-sec | kpc | arc-sec | kpc | | arc-sec | kpc | |
| NGC 2683 | 130 \pm 24 | 4.8 \pm 0.9 | 21 \pm 8 | 0.8 \pm 0.3 | 6.2 \pm 2.6 | 21 \pm 7 | 0.8 \pm 0.3 | 6.2 \pm 2.3 |
| NGC 3627 | 120 \pm 24 | 6.0 \pm 1.2 | – | – | – | 20 \pm 4 | 1.0 \pm 0.2 | 6.0 \pm 1.7 |
| NGC 4096 | 53 \pm 15 | 2.1 \pm 0.6 | 31 \pm 10 | 1.2 \pm 0.4 | 1.7 \pm 0.7 | < 32'' | < 1.3 | >1.6 |
| NGC 4449 | 90 \pm 12 | 1.8 \pm 0.25 | – | – | – | 62 \pm 10 | 1.3 \pm 0.2 | 1.4 \pm 0.3 |
| NGC 4490 | 86 \pm 17 | 3.3 \pm 0.7 | 55 \pm 8 | 2.1 \pm 0.3 | 1.6 \pm 0.4 | – | – | – |
| NGC 4826 | – | – | – | – | – | – | – | – |
| NGC 5194 | 150 \pm 10 | 6.1 \pm 0.4 | 75 \pm 10 | 3.1 \pm 0.4 | 2.0 \pm 0.3 | – | – | – |

Table 4. Fitted values of the radio-FIR correlation at 0.33 and 1.4 GHz of the sample galaxies.

| Name | b (0.33 GHz) | b (1.4 GHz) | log(a) [0.33 GHz] [log(Jy/Beam)] | log(a) [1.4 GHz] [log(Jy/Beam)] | Scatter (0.33 GHz) [log(Jy/Beam)] | Scatter (1.4 GHz) [log(Jy/Beam)] |
|---------------------|-----------------|-----------------|-------------------------------------|------------------------------------|--------------------------------------|-------------------------------------|
| NGC 2683 | 0.54 \pm 0.06 | 0.91 \pm 0.07 | -2.29 \pm 0.04 | -2.47 \pm 0.05 | 0.07 | 0.08 |
| NGC 3627 | 0.55 \pm 0.03 | 0.85 \pm 0.13 | -1.78 \pm 0.02 | -2.5 \pm 0.05 | 0.13 | 0.12 |
| NGC 4096 | 0.74 \pm 0.05 | 0.90 \pm 0.04 | -2.01 \pm 0.04 | -2.35 \pm 0.04 | 0.10 | 0.10 |
| NGC 4449 | 0.77 \pm 0.05 | 0.65 \pm 0.04 | -2.14 \pm 0.03 | -2.35 \pm 0.02 | 0.13 | 0.12 |
| NGC 4490 | 0.68 \pm 0.02 | 0.75 \pm 0.02 | -1.62 \pm 0.02 | -1.94 \pm 0.01 | 0.12 | 0.11 |
| NGC 4826 | 1.39 \pm 0.1 | 1.47 \pm 0.08 | -2.78 \pm 0.05 | -2.93 \pm 0.04 | 0.09 | 0.11 |
| NGC 5194 (arm) | 0.50 \pm 0.05 | 0.65 \pm 0.04 | -1.85 \pm 0.02 | -2.23 \pm 0.02 | 0.16 | 0.17 |
| NGC 5194 (interarm) | 0.73 \pm 0.11 | 1.03 \pm 0.05 | -1.74 \pm 0.05 | -2.12 \pm 0.04 | 0.15 | 0.19 |

**Figure 32.** 70 μ m FIR vs 0.33 and 1.4 GHz radio intensity (lower plot) of NGC 4096. To the 0.33 GHz data 0.5 dex has been added.

and is ~ 4.3 between 0.33 and ~ 6 GHz. From Table-3, we find that for NGC 4096 and 4490, the ratios of the FWHMs from P and L/C band are consistent (given the errors) with the simple diffusion scenario. For NGC 3627 and 5194, the ratio of convolution FWHM from the P-band (ν_1) and C or/and L-band (ν_2), is consistent with streaming instability. This mechanism is also consistent with CRE propagation scale found above from the 0.14 GHz thermal subtracted LOFAR image (Sect. 4.3) for NGC 5194. It is however at variance with the detailed modelling of CRE propagation in this galaxy (Mulcahy et al. 2016). For NGC 2683, kernel FWHM in L and C band remains the same, but increases by a factor of 6 in P band. Reconciling these three results from a physically intuitive scenario is not possible. Given the higher structural sensitivity of the C band image as compared to

**Figure 33.** 70 μ m FIR vs 0.33 and 1.4 GHz radio intensity (lower plot) of NGC 4449. To the 0.33 GHz data 0.5 dex has been added.

the L band one, we only consider the ratio of FWHMs from P and C band images from Table-3, which is consistent with CRE propagation due to streaming instability. Further observations would be needed to confirm the ratio of FWHMs of CRE propagation between L and P band for this galaxy. For NGC 4449, the ratio of CRE propagation FWHMs from P and C band is ~ 1 , suggestive of galactic outflow (diffusion could explain it if the measured ratio (Table-3) is off by 2σ). This could not be caused by lack of short uv -spacing or low sensitivity in P band, but it needs to be verified by independent observations and analysis.

It should be noted that diffusion is expected to happen in all galaxies at large length scales (\gtrsim tens of kpcs), but indications of the other mechanisms have been suggested in literature. Streaming instability is indicated in NGC

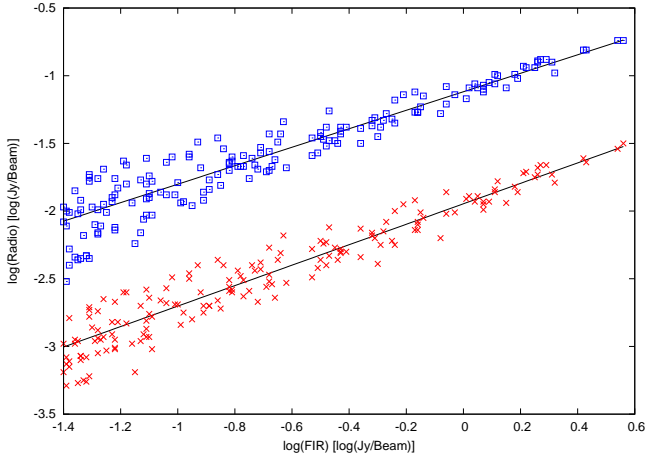


Figure 34. $70\ \mu\text{m}$ FIR vs 0.33 and 1.4 GHz radio intensity (lower plot) of NGC 4490. To the 0.33 GHz data 0.5 dex has been added.

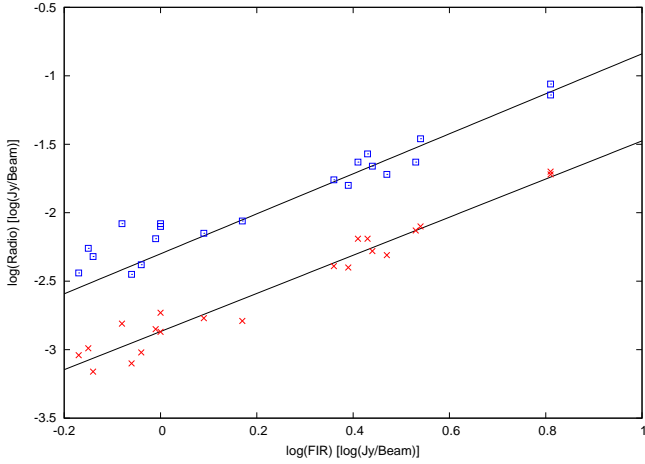


Figure 35. $70\ \mu\text{m}$ FIR vs 0.33 and 1.4 GHz radio intensity (lower plot) of NGC 4826. To the 0.33 GHz data 0.5 dex has been added.

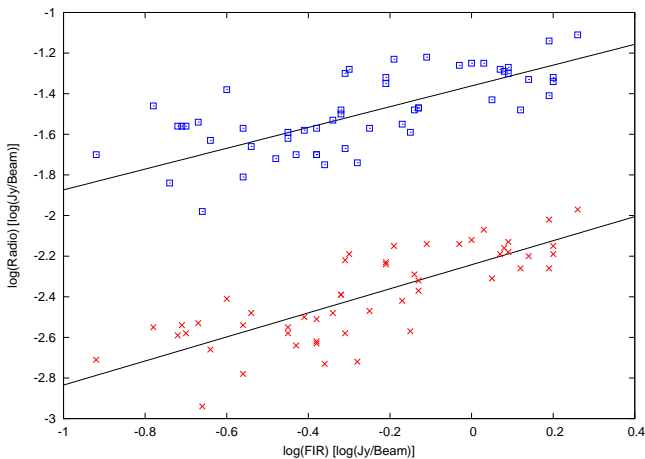


Figure 36. $70\ \mu\text{m}$ FIR vs 0.33 and 1.4 GHz radio intensity (lower plot) in the arm region of NGC 5194. To the 0.33 GHz data 0.5 dex has been added.

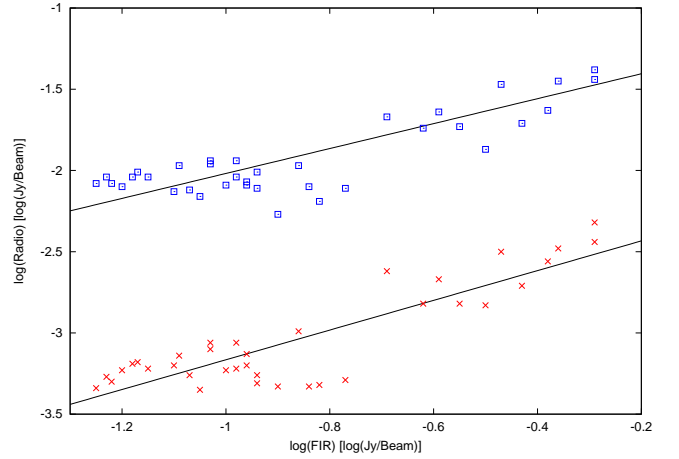


Figure 37. $70\ \mu\text{m}$ FIR vs 0.33 and 1.4 GHz radio intensity (lower plot) in the interarm region of NGC 5194. To the 0.33 GHz data 0.5 dex has been added.

1097, NGC 5055 and IC 342 (Basu & Roy 2013; Beck 2015). Heesen et al. (2018) present cases of 11 galaxies where advection (galactic outflows) plays the dominant role. Diffusion is indicated in NGC 4736, NGC 5236, NGC 6946 and NGC 5194 (Basu & Roy 2013; Mulcahy et al. 2016). We have made several assumptions on the properties of the convolution kernel. While determining the FWHM of the convolution kernel, we assumed that the exponent of radio-FIR correlation is unity, which is not true for galaxies with significant escape of CReS. A more plausible solution would involve model of a galaxy and numerical simulation involving different physical models of CRe propagation and then finding a generic solution as a combination of all these processes. While fitting the data for correlation between radio and convolved FIR maps, we had to apply lower and in many cases upper cut-offs to the data, which are somewhat subjective in nature. FIR images with higher resolution, better technique to analyse the images and a larger sample size would be needed to get a better handle in unravelling the mechanisms of CRe propagation in nearby normal galaxies. Such a process would be attempted in future involving a larger number of galaxies from our original sample.

5.2 Low frequency radio-FIR correlation

CReS with lower energy propagate a longer distance in their lifetime than their higher energy counterparts. In a typical magnetic field of $10\ \mu\text{G}$, the peak emission at 1.4 GHz would occur from electrons with energy $\sim 3\ \text{GeV}$, and has a typical lifetime of $\sim 2.5 \times 10^7$ years. In this timescale, they could propagate to a distance of $\sim 1\ \text{kpc}$. With the above magnetic fields for the 1.5 GeV electrons, they would survive twice longer and could propagate to a distance of $\sim 2\ \text{kpc}$ during their lifetime. From our sample, the average exponent of the correlation between 0.33 GHz radio and $70\ \mu\text{m}$ FIR is 0.78 ± 0.1 (for NGC 5194, we only considered the exponent from the arm regions). The galaxy NGC 4826 in the sample has an anomalously high exponent of 1.39 at 0.33 GHz. As mentioned earlier in Sect. 4.3, a large part of the emission originates from the core region of the galaxy that may have a different ratio of radio to FIR emission, which would affect

the exponent of the radio-FIR correlation. Also, there could be significant AGN contribution to the emission from the core. Therefore, the exponent of radio-FIR correlation for this galaxy needs to be used with caution. Its exponent of radio-FIR correlation well above unity is, however, consistent with the non-calorimeter model (Niklas & Beck 1997). If this galaxy is excluded from Table-4, the mean exponent is 0.63 ± 0.06 . This exponent at 0.33 GHz is significantly lower than 0.78 ± 0.04 obtained using 1.4 GHz data for the same galaxies. Since CRe propagate significantly further than the linear resolution of our observations at 0.33 GHz, this would cause the radio-FIR correlation to flatten from 0.33 GHz radio maps as compared to 1.4 GHz, and can explain the above result. However, we note that the above trend is not seen from 0.33 and 1.4 GHz maps of NGC 4449 (see Table-4). As noted in Sect. 4.3, 1.4 GHz image of NGC 4449 made from VLA archival data has poorer structural sensitivity than the 0.33 GHz image. Consequently, 'b' value measured using the 1.4 GHz emission would arise from much smaller core regions of the 0.33 GHz emission, and the two results cannot be compared. We also consider the exponent obtained from our 0.33 GHz observation with Basu et al. (2012b). Considering that most of galactic emission in spirals originates from arm regions, we find from Table-3 of Basu et al. (2012b) the 0.33 GHz radio to 70 μm FIR average exponent is 0.57 ± 0.05 for their sample of 4 galaxies. For NGC 5194, spatially separated radio-FIR correlation for the arm and interarm regions are shown in Fig. 36 and 37. Contrary to what was found by Basu et al. (2012b) for other large face-on galaxies, we do not observe any significant flattening of the exponent for the interarm region for this galaxy at 0.33 and 1.4 GHz. At 0.33 GHz, the exponent for the interarm region is 0.73 ± 0.11 , which is way steeper than the average exponent of 0.33 ± 0.02 found for the interarm regions of the four nearby spirals (Basu et al. 2012b).

6 CONCLUSIONS

(i) We have observed a set of seven galaxies NGC 2683, NGC 3627, NGC 4096, NGC 4449, NGC 4490, NGC 4826 and NGC 5194 within 11 Mpc at 0.33 GHz using GMRT and also analysed their archival higher radio frequency data at 1.4 or ~ 6 GHz. Their total intensity and non-thermal spectral index maps are presented here. Radio maps for most of these galaxies were not available below 1 GHz with high resolution ($\sim 10''$) and sub-mJy sensitivity.

(ii) The spectral indices of the galaxies are typically flat at the centre and in compact star forming regions. It gradually steepen with increasing galactocentric distances.

(iii) To determine the characteristic smearing scales due to propagation of CRe in galaxies at different radio bands, we assumed a simple isotropic diffusion model, and convolved the 70 μm FIR maps of the galaxies with Gaussian kernels with different angular sizes till the exponent of their radio-FIR correlation reached unity. CRe propagation in NGC 4096 and 4490 could be explained by the simple diffusion scenario. For NGC 2683, 3627 and 5194, CRe propagation through streaming instability could explain the results. For NGC 4449, propagation through galactic outflow is suggested.

(iv) We have studied spatially resolved radio-FIR correl-

ation between 0.33, 1.4 GHz radio and 70 μm FIR emission. The average exponent of the radio-FIR correlation for six of the galaxies is found to be 0.63 ± 0.06 using radio maps at 0.33 GHz, and is quite close to the average exponent of 0.57 ± 0.05 obtained for the arm regions of 4 nearby large spirals (Basu et al. 2012b).

APPENDIX

CRe propagation from a compact source due to isotropic diffusion

Outflow (J) at a distance 'r' from a source can be written as $J(r) = -D \frac{dn}{dr}$, where $\frac{dn}{dr}$ is the net density gradient of CRe, and D is the diffusion coefficient considered constant. Also, $\frac{\delta n}{\delta t} = \frac{\delta J}{\delta r}$. The solution of which is

$$n(r, t) = \frac{N}{\sqrt{4\pi Dt}} \exp\left(-\frac{r^2}{4Dt}\right)$$

where, N is the rate of CRe generation from source. After a long time (more than synchrotron lifetime) when steady state is reached, observed density would be the integrated value of the above for all the CRe emission over time from start ($t = 0$) to the lifetime of synchrotron emission ($t = \tau_\nu$).

$$n_\nu(r) = \frac{2N_\nu}{\sqrt{\pi D}} \int_0^{\tau_\nu} \frac{1}{\sqrt{t}} \exp\left(-\frac{r^2}{4Dt}\right) dt$$

where we have considered N_ν and n_ν are the rate of CRe production and the density of CRe whose peak emission occurs at a frequency ν , and lifetime of synchrotron emission is τ_ν . The integrated value of the above equation is

$$n_\nu(r) = \frac{2N_\nu}{\sqrt{\pi D}} \left(\sqrt{\tau_\nu} \exp\left(-\frac{r^2}{4D\tau_\nu}\right) - r \sqrt{\frac{\pi}{4D}} \operatorname{erf}\left(\frac{r}{\sqrt{4D\tau_\nu}}\right) \right)$$

Considering emission at 0.33 GHz, the typical astrophysical values of r is $\sim \text{kpc}$, $\tau_\nu \sim 10^8$ yr and $D \sim 10^{28} \text{ cm}^2 \text{ sec}^{-1}$. It can then be shown that typically the first term (before the negative sign) dominates, which indicates a Gaussian profile of CRe density distribution as a function of distance from the source.

ACKNOWLEDGEMENTS

We thank Dipanjan Mitra for reading the manuscript and providing useful comments. We also thank the anonymous referee for important comments which helped to improve the quality of the paper and to avoid certain significant errors. We thank the staff of GMRT that allowed these observations to be made. GMRT is run by National Centre for Radio Astrophysics of the Tata Institute of fundamental research. We acknowledge support of the Department of Atomic Energy, Government of India, under project no. 12-R&D-TFR-5.02-0700.

DATA AVAILABILITY

The raw interferometric data at 0.33 GHz used in this paper is publicly available from the GMRT Online Archive at <https://naps.ncra.tifr.res.in/goa> (Project: 29_088). Advanced

data products used in the article will be shared on reasonable request to the corresponding author.

References

- Amato E., Blasi P., 2018, *Advances in Space Research*, **62**, 2731
- Basu A., Roy S., 2013, *MNRAS*, **433**, 1675
- Basu A., Mitra D., Wadadekar Y., Ishwara-Chandra C. H., 2012a, *MNRAS*, **419**, 1136
- Basu A., Roy S., Mitra D., 2012b, *ApJ*, **756**, 141
- Basu A., Beck R., Schmidt P., Roy S., 2015, *MNRAS*, **449**, 3879
- Beck R., 2015, *A&A*, **578**, A93
- Beck R., Graeve R., 1982, *A&A*, **105**, 192
- Beck R., Berkhuijsen E. M., Gießübel R., Mulcahy D. D., 2020, *A&A*, **633**, A5
- Bell A. R., 1978, *MNRAS*, **182**, 147
- Berkhuijsen E. M., Beck R., Hoernes P., 2003, *A&A*, **398**, 937
- Berkhuijsen E. M., Beck R., Tabatabaei F. S., 2013, *MNRAS*, **435**, 1598
- Bicay M. D., Helou G., 1990, *ApJ*, **362**, 59
- Biermann P. L., Strom R. G., 1993, *A&A*, **275**, 659
- Braun R., Walterbos R. A. M., Kennicutt Robert C. J., 1992, *Nature*, **360**, 442
- Braun R., Oosterloo T. A., Morganti R., Klein U., Beck R., 2007, *A&A*, **461**, 455
- Chyży K. T., Beck R., Kohle S., Klein U., Urbanik M., 2000, *A&A*, **355**, 128
- Condon J. J., 1987, *ApJS*, **65**, 485
- Condon J. J., 1992, *ARA&A*, **30**, 575
- Dale D. A., et al., 2009, *ApJ*, **703**, 517
- Dressel L. L., 1988, *ApJ*, **329**, L69
- Dumas G., Mundell C. G., Emsellem E., Nagar N. M., 2007, *MNRAS*, **379**, 1249
- Dumas G., Schinnerer E., Tabatabaei F. S., Beck R., Velusamy T., Murphy E., 2011, *AJ*, **141**, 41
- Ginzburg V. L., Syrovatskii S. I., 1965, *ARA&A*, **3**, 297
- Heesen V., et al., 2018, *MNRAS*, **476**, 158
- Heesen V., et al., 2019, *A&A*, **622**, A8
- Helou G., Soifer B. T., Rowan-Robinson M., 1985, *ApJ*, **298**, L7
- Helou G., Khan I. R., Malek L., Boehmer L., 1988, *ApJS*, **68**, 151
- Hoernes P., Berkhuijsen E. M., Xu C., 1998, *A&A*, **334**, 57
- Hughes A., Wong T., Ekers R., Staveley-Smith L., Filipovic M., Maddison S., Fukui Y., Mizuno N., 2006, *MNRAS*, **370**, 363
- Hummel E., 1981, *A&A*, **93**, 93
- Hummel E., 1991, in Bloemen H., ed., *IAU Symposium Vol. 144, The Interstellar Disk-Halo Connection in Galaxies*. p. 257
- Hummel E., Dettmar R. J., 1990, *A&A*, **236**, 33
- Hummel E., van der Hulst J. M., 1989, *A&AS*, **81**, 51
- Intema H. T., 2014, SPAM: Source Peeling and Atmospheric Modeling (ascl:1408.006)
- Irwin J., et al., 2012, *AJ*, **144**, 44
- Karczewski O. L., et al., 2013, *MNRAS*, **431**, 2493
- Kennicutt Robert C. J., et al., 2003, *PASP*, **115**, 928
- Kennicutt Robert C. J., Lee J. C., Funes J. G., J. S., Sakai S., Akiyama S., 2008, *ApJS*, **178**, 247
- Kennicutt R. C., et al., 2011, *PASP*, **123**, 1347
- Krause M., et al., 2018, *A&A*, **611**, A72
- Lang K. R., Terzian Y., 1969, *Astrophys. Lett.*, **3**, 29
- Lawrence A., Kerton C. R., Struck C., Smith B. J., 2020, *The Astrophysical Journal*, **891**, 11
- Lerche I., Schlickeiser R., 1982, *A&A*, **107**, 148
- Lisenfeld U., Voelk H. J., Xu C., 1996, *A&A*, **306**, 677
- Madden S. C., et al., 2013, *PASP*, **125**, 600
- Mulcahy D. D., et al., 2014, *A&A*, **568**, A74
- Mulcahy D. D., Fletcher A., Beck R., Mitra D., Scaife A. M. M., 2016, *A&A*, **592**, A123
- Murgia M., Helfer T. T., Ekers R., Blitz L., Moscadelli L., Wong T., Paladino R., 2005, *A&A*, **437**, 389
- Murphy E. J., et al., 2006, *ApJ*, **638**, 157
- Nikiel-Wroczyński B., Jamrozy M., Soida M., Urbanik M., Knapik J., 2016, *MNRAS*, **459**, 683
- Niklas S., Beck R., 1997, *A&A*, **320**, 54
- Paladino R., Murgia M., Orrù E., 2009, *A&A*, **503**, 747
- Price R., Duric N., 1992, *ApJ*, **401**, 81
- Ptuskin V. S., 2001, *Space Sci. Rev.*, **99**, 281
- Rossa J., Dettmar R. J., 2003, *A&A*, **406**, 493
- Rubin R. H., 1968, *ApJ*, **154**, 391
- Soida M., Urbanik M., Beck R., Wielebinski R., Balkowski C., 2001, *A&A*, **378**, 40
- Sramek R., 1975, *AJ*, **80**, 771
- Srivastava S., Kantharia N. G., Basu A., Srivastava D. C., Ananthakrishnan S., 2014, *MNRAS*, **443**, 860
- Swarup G., Ananthakrishnan S., Kapahi V. K., Rao A. P., Subrahmanya C. R., Kulkarni V. K., 1991, *CURRENT SCIENCE* V.60, NO.2/JAN25, P. 95, 1991, 60, 95+
- Tabatabaei F. S., Krause M., Beck R., 2007a, *A&A*, **472**, 785
- Tabatabaei F. S., Beck R., Krügel E., Krause M., Berkhuijsen E. M., Gordon K. D., Menten K. M., 2007b, *A&A*, **475**, 133
- Tabatabaei F. S., Berkhuijsen E. M., Frick P., Beck R., Schinnerer E., 2013, *A&A*, **557**, A129
- Voelk H. J., 1989, *A&A*, **218**, 67
- Vollmer B., Soida M., Beck R., Powalka M., 2020, *A&A*, **633**, A144
- Wakker B. P., Schwarz U. J., 1988, *A&A*, **200**, 312
- Wiegert T., et al., 2015, *AJ*, **150**
- Wunderlich E., Klein U., Wielebinski R., 1987, *A&AS*, **69**, 487
- Xu C., Klein U., Meinert D., Wielebinski R., Haynes R. F., 1992, *A&A*, **257**, 47
- Yun M. S., Reddy N. A., Condon J. J., 2001, *ApJ*, **554**, 803
- van der Kruit P. C., 1971, *A&A*, **15**, 110
- van der Kruit P. C., Allen R. J., Rots A. H., 1977, *A&A*, **55**, 421

Supplementary material for Low radio frequency observations of seven nearby galaxies with GMRT

Subhashis Roy¹  Souvik Manna¹

¹National Center for Radio Astrophysics, TIFR, Pune University Campus, Ganeshkhind, Pune 411007, India

26th August 2021

arXiv:2108.10909v1 [astro-ph.GA] 24 Aug 2021

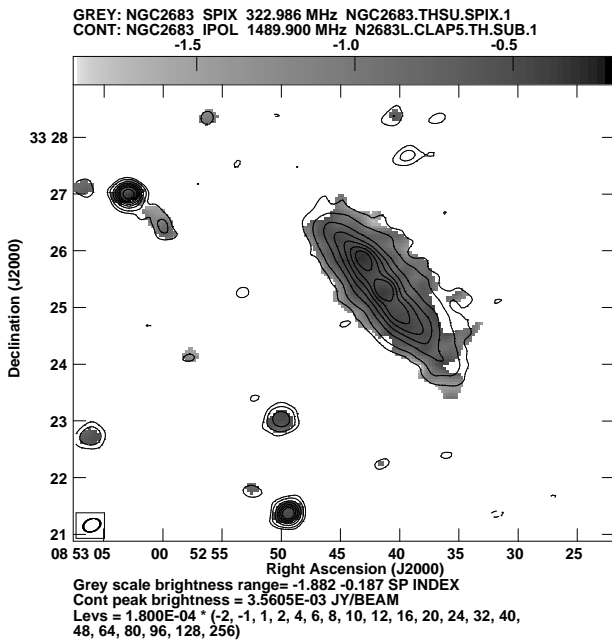


Figure 1. Thermal emission subtracted 1.4 GHz map (contour) and non-thermal spectral index of NGC 2683 (gray). Resolution is $19'' \times 13''$.

NON-THERMAL SPECTRAL INDEX IMAGES OF NGC 2683, 3627, 4096 AND 4449 BETWEEN 1.4 AND 0.33 GHz AND THEIR THERMAL EMISSION SUBTRACTED 1.4 GHz MAPS

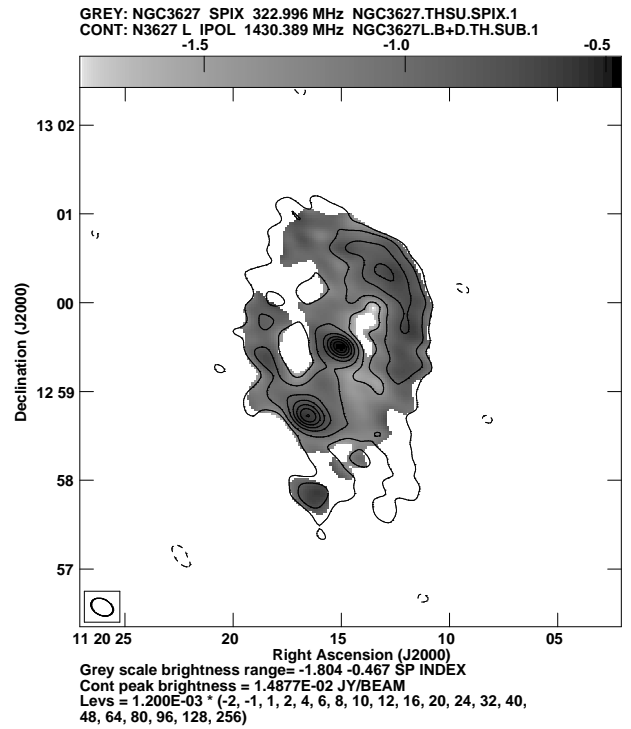


Figure 2. Thermal emission subtracted 1.4 GHz map (contour) and non-thermal spectral index of NGC 3627 (gray). Resolution is $16'' \times 11''$.

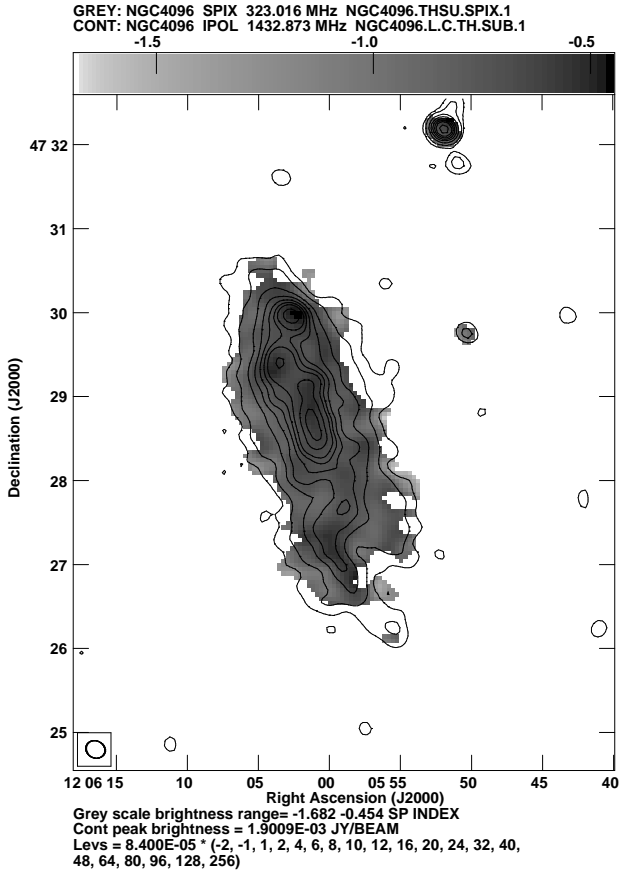


Figure 3. Thermal emission subtracted 1.4 GHz map (contour) and non-thermal spectral index of NGC 4096 (gray). Resolution is $14'' \times 12''$.

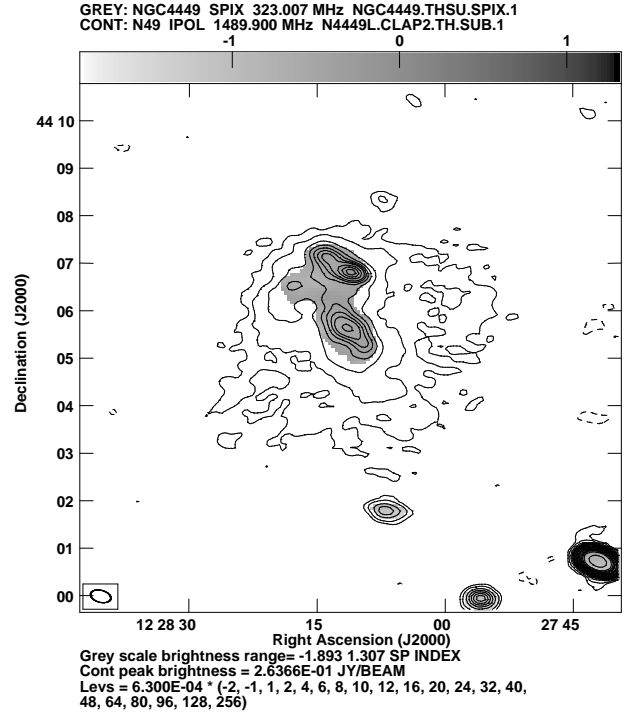


Figure 4. Thermal emission subtracted 1.4 GHz map (contour) and non-thermal spectral index of NGC 4449 (gray). Resolution is $26.1'' \times 15''$.